Kobe University Repository : Kernel

PDF issue: 2026-11-05

Nuclear Magnetic Resonance and Surface Impedance Studies of Heavy Fermion Superconductor UBe[13]

Matsuno, Haruki

(Degree)
博士（理学）

(Date of Degree)
2017-03-25

(Date of Publication)
2021-03-25

(Resource Type)
doctoral thesis

(Report Number)
甲第6848号

(URL)
https://hdl.handle.net/20.500.14094/D1006848

※ 当コンテンツは神戸大学の学術成果です。無断複製・不正使用等を禁じます。著作権法で認められている範囲内で、適切にご利用ください。

Doctoral Dissertation

Nuclear Magnetic Resonance and Surface Impedance Studies of Heavy Fermion Superconductor UBe_{13}

January 2017

Graduate School of Science, Kobe University

Haruki Matsuno

松野　治貴

Abstract

The heavy fermion superconductor UBe_{13} attracts much attention because of the intriguing physical properties in the normal and superconducting states. This material exhibits superconductivity at $T_c = 0.86$ K. Although a number of experimental and theoretical studies have been made to clarify its unusual physical properties in UBe_{13} over the past three decades, many issues to be clarified, e.g. the symmetry of Cooper pairing, the superconducting properties, etc. still remain at present.

In the normal state of UBe_{13}, many experimental and theoretical works have pointed out its unusual physical properties. The electronic specific heat coefficient γ is extremely large ($\sim 1100\mathrm{mJ/mol \cdot K^2}$) caused by heavy quasiparticles. The temperature dependence of the electric resistivity shows logarithmic temperature dependence of $\rho \propto -\ln T$ above 30 K, associated with the single impurity Kondo effect. On the other hand, even at low temperature, the temperature dependence of the resistivity does not follow $\rho(T) \propto T^2$-law, which is expected for the heavy Fermi liquid state, and the large value of $\rho \approx 100\,\mu\Omega$cm remains just above T_c. It has been discussed that a non-Fermi liquid state is realized at low temperatures above T_c.

The superconducting properties of UBe_{13} is also strange. A very large specific heat jump is observed just below T_c, indicating that the heavy quasiparticles are responsible for superconductivity. The magnetic field dependence of specific heat reveals an anomaly in superconducting state. This anomaly has been observed by means of other measurements, for example, surface impedance, magnetization, and nuclear magnetic resonance (NMR) experiments. To understand these results, some scenarios have been proposed. However, the origin of this anomaly is not clear yet.

In order to clarify such novel normal and superconducting properties in UBe_{13}, in particular, the symmetry of the superconducting order parameter, and the origin of the anomaly at T_a which appears in the superconducting state, we have carried out ^{9}Be-NMR and surface impedance measurements for a single crystal UBe_{13} down to 0.03 K using a ^{3}He-^{4}He dilution refrigerator. The external field was applied by solenoid type superconducting magnet up to 10 T. The surface impedance measurements have been carried out at various temperatures and frequencies. The NMR measurements have been carried out by using the conventional phase-coherent NMR

spectrometers using Hahn spin-echo method. The temperature dependences of Knight shift and nuclear spin-lattice relaxation rate at various fields have been measured.

The surface impedance measurements demonstrate the anomalous field dependence of the surface resistance R_s in the superconducting state, which is quite different from other heavy fermion compounds. In order to investigate the anomaly in R_s, the frequency dependences about 6.3, 29, 71 and 97 MHz have been measured. These measurements reveal that two characteristic flux pinning mechanisms exist. One is the conventional flux pinning which appears in the low field region and the pinning frequency is estimated to be $\omega_{p1} < 30$ MHz. Such a flux pinning ω_{p1} associates with impurities or/and defects. The other is the unusual flux pinning which appears at high field region. Such an unusual flux pinning doesn't appear at 71 MHz. This result indicates that the pinning frequency is of $30 < \omega_{p2} \ll 71$ MHz. Furthermore, we also found that $R_s(H)$ is independent of observed frequency above 71 MHz, indicating that the free flux flow state is realized above 71 MHz. However, the drastic change of R_s below H_{c2} remains even above 71 MHz. These results indicate that the charge of R_s below H_{c2} is attributed to the other mechanisms than the "conventional" pinning effect. A possible explanation for unusual behavior of R_s is that the flux flow resistivity ρ_f changes. The ρ_f is associated with the lifetime of quasiparticle τ, carrier density of quasiparticle in the core of vortex, n, and the gap structure around the vortex, $\langle\omega(k)\rangle$. In order to explain the behavior of R_s around the H_{c2}, either the parameters of $\langle\omega(k)\rangle$, τ, n should become large with decreasing field from H_{c2}. By taking the results of Knight shift into consideration, the anomaly of R_s can be explained by the change of τ.

^{9}Be-NMR measurements have been carried out to clarify the superconducting anomalies from microscopic viewpoints. From the ^{9}Be NMR spectrum and its line analyses, the NMR and nuclear quadrupole parameters was obtained for two Be sites of Be(I) and Be(II) sites. The NMR Knight shift for the Be(II) shows unusual shift at T_a below T_c. The NMR spectra broaden except the spectrum under 5.47 T for $H\|$ [111]. Such a spectral broadening cannot be explained by the effect of the vortex lattice in the superconducting mixed state, where the distribution of local field is caused by the vortex lattice, the so called "Redfield NMR pattern". The spectral broadening below T_a is larger than the calculated Redfield pattern.

The Knight shift of Be(II) under 3 and 4 T parallel to [111] exhibits clear reduction

below T_a. On the other hand, the Knight shift of Be(I) show no change down to the lowest temperature. If the anomalous reduction observed in the Be(II) Knight shift at T_a relates to the change of the superconducting state, the spectra of Be(I) site should change below T_a as same as that of Be(II) site. However, the peak position and line width of the Be(I) site under the fields of 3 T and 4 T show no change below T_a. Thus, these results indicate that the origin of the anomaly does not relate to superconductivity. A possible explanation is some magnetic ordering. If an antiferromagnetic like order occurs at T_a, the internal field affects the electronic state at Be(II) site. On the other hand, at Be(I) site, which locates in cubic symmetry, the internal field can be canceled and we expect no change of the Knight shift. This scenario is consistent with the results of the surface impedance measurements.

It is necessary to understand the ground state of UBe_{13} to consider what kind of ordering occurs. However, the CEF state of UBe_{13} is not clear because of the itinerant nature of 5*f*-electron state. Theoretically, either Γ_3 CEF doublet or Γ_1 CEF singlet ground state has been proposed. The former CEF ground state has multipoles degree of freedom, such as quadrupole and octupoles. The later singlet ground state is magnetically intact and leads no magnetic and electric orderings. However, when the Γ_5 CEF first-excited magnetic triplet state, which stays closely to the ground state level, is taken into account, the quasi-degenerated quartet sate has also multipoles degree of freedom, such as quadrupoles, octupoles and hexadecapoles. Considering with the results of neutron scattering experiments, which observed an antiferromagnetic fluctuations, an antiferro octupole ordering is a possible candidate account for the anomalous behavior of the Knight shift in UBe_{13}.

This scenario can explain the anomalies in the superconducting state observed by the surface impedance and NMR results. Therefore, the present results indicate that the Knight shift in the superconducting state does no change at all on passing through both T_c and T_a. This result strongly suggests that the spin triplet superconducting state is realized in UBe_{13}.

Finally, we discuss the temperature dependence of $1/T_1$, which is in proportion to $T^2 \sim T^3$ at low $T(\ll T_c)$. This result suggests that UBe_{13} has either the nodal gap with line node at Fermi surface or multi-band full gap as reported by Iron Pnictides. The field dependence of $1/T_1$ which is expected in superconductor with nodal gap cannot be observed. This behavior is reminiscent of that for the iron pnictides and

suggests that the superconducting gap is expected to be a multi-band full-gap state. However, we cannot conclude the superconducting gap structure at the present stage.

Instead we claim that the superconducting state of UBe_{13} is unusual associated with the multi $5f$-orbitals having multipole degrees of freedom, as well as the nature of multiband in UBe_{13}.

Contents

1 Overview 1

1.1 Heavy fermion system 1

1.2 Fermi liquid 3

1.3 Superconductivity 4

1.3.1 Parity of superconductivity 5

1.3.2 Superconducting order parameter 6

2 Introduction 8

2.1 Crystal structure 8

2.2 Unusual physical properties in the normal state 8

2.3 Unconventional superconductivity 11

2.3.1 Superconducting gap 11

2.3.2 Superconducting upper critical field $H_{c2}(T)$ 11

2.3.3 Anomaly in the superconducting state 11

2.3.4 NMR and μSR 12

3 Purpose 14

4 Experimental procedure 15

4.1 Sample 15

4.2 Apparatuses 15

4.2.1 NMR apparatus 15

4.2.2 Superconducting magnets 16

4.2.3 Cryostats 17

5 Introduction to NMR and Surface Impedance 19

5.1 Hyperfine interaction and nuclear quadrupole interaction 19

5.1.1 NMR spectrum 20

5.1.2 Knight shift and local field 22

5.2 Surface impedance measurements 23

5.2.1 Theoretical back ground 23

5.2.2 RF surface impedance measurement 24
5.2.3 Surface impedance in the superconducting state 26
5.2.4 Pinning effect 27

6 Result 29
6.1 Surface impedance 29
6.2 NMR 35
6.2.1 H // [111] 35
6.2.2 H//[110] 43
6.2.3 H//[001] 49
6.2.4 The nuclear relaxation rate $1/T_1$ 55

7 Discussion 57
7.1 The frequency dependence of Rs 57
7.2 NMR 61
7.2.1 Normal state 61
7.2.2 superconducting state 62
7.3 Superconductivity symmetry 72

8 Conclusion 75

1 Overview

UBe_{13} is a heavy fermion superconductor which was discovered in 1983 by Ott *et al.* and shows unusual normal and superconducting properties that are different from other heavy fermion compounds. Although various experiments have been performed for three decades since the discovery, the nature of UBe_{13} has not been revealed yet[1].

1.1 Heavy fermion system

For example, physical properties of a simple metal e.g. Al, can be explained by free electron model, where the Coulomb repulsion among electrons can work only in short range because of the screening by other electrons. On the other hand, the intermetallic compounds including transition metal, lanthanoid and actinoid have electrons in narrow band originated from d or f orbital. Hence, the Coulomb repulsion affects strongly and the complex physical properties which are different from free electron system are observed. When $4f$ or $5f$ orbitals consist of conduction bands, the Coulomb repulsion among conduction electrons works strongly and their localized character is prominent. The interaction between localized electrons and conduction electrons, is described as sd exchange interaction $\mathcal{H}_{sd} = J_{sd}\vec{s}\cdot\vec{S}$ in d electron system. Here, $\vec{s}$ and $\vec{S}$ are conduction and localized electron spins, respectively. In f electron system, it is described as $\mathcal{H}_{cf} = J_{cf}\vec{s}\cdot\vec{J}$. Here, $\vec{J}$ is total angular momentum. These exchange interactions play important role in their physical properties at low temperatures. In the low temperature region, the exchange interaction causes two different effects. One is the Kondo effect and the other is the Rudermann-Kittel-Kasuya-Yosida (RKKY) interaction. The Kondo effect brings about non-magnetic state, where localized spins are screened by conduction electrons. On the other hand, the magnetic order state is stabilized by the RKKY interaction which causes polarization of conduction electrons.

In the Ce or U compounds, f electrons behave localized spin at high temperature region (figure 1.1(b)). In the low temperature region, due to the mixing of conduction electrons and localized f electrons, spin-singlet state is formed via Kondo effect（figure 1.1(a)). This singlet is called the Kondo singlet and its characteristic temperature is defined as T_K. When magnetic ions are set periodically in array and form the lattice,

the effective wave function of the Kondo singlet, namely the Kondo cloud, can be overlapped. For that reason, the f electrons have a slightly itinerant character (figure 1.1(c)). At the same time, the effective mass m^* is enhanced by several hundred times with respect to the bare electron mass m_0. Hence, such compounds are called as "Heavy fermion system".

Furthermore, when the RKKY interaction is taken into consideration, a magnetic correlation cannot be ignored. Thus, the competition of Kondo effect and RKKY interaction causes various ground states. This concept was suggested by Doniach and summarized as Doniach phase diagram. Moreover, f electron system has a degree of freedom of orbitals. Thus, more complex ground state can be realized e.g., ferromagnetic, antiferromagnetic, multipole order, Non-Fermi-liquid state or heavy fermion superconductivity etc. Thus, physics of heavy fermion system is one of central issues in condensed matters. Especially, heavy fermion system has various physical properties depending on their electronic state of the ground state.

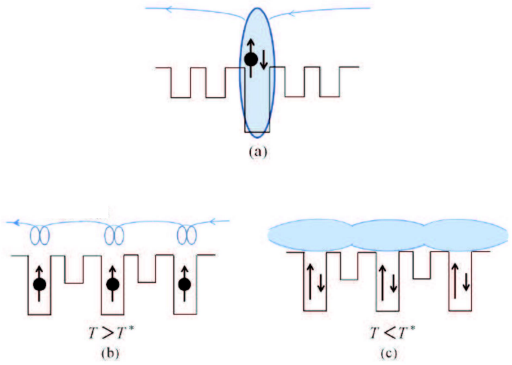


Figure1.1 (a)impurity Kondo effect (b)Interaction of conduction and local electron (c)The image of heavy fermion state[2]

1.2 Fermi liquid

Heavy fermion system in which strong electronic correlation works among electrons can be described by Landau Fermi liquid theory. This theory explains the ground state properties and its low energy excitations in correlated electron system. However, the physical properties, such as specific heat coefficient and susceptibility, of a Fermi liquid state resemble those of free electron system. The mass of correlated electrons in the Fermi liquid state is not expressed by m_0 ($= 9.1056 \times 10^{-28}$ g) but is rather replaced by "effective mass" m^* that is enhanced by correlations. Namely, conduction electrons are no longer "free" but are dressed in "clothes" of correlations among electrons, the so called "quasiparticles". In the Fermi liquid state, resistivity, specific heat coefficient and susceptibility are expressed by $\rho = AT^2 \propto m_0^2 T^2$, specific heat coefficient, $C/T = \gamma \propto m_0^2$, and susceptibility $\chi \propto m_0$. In the heavy fermion system, the basic physical properties can be also described by the Landau Fermi Liquid theory with the "heavy" effective mass, where the effective mass is enhanced by, typically, several hundreds, $m^* \approx 10^2 m_0$ via exchange interaction between the conduction electron and localized electron. Two or three dimensional metal can be explained by this theory at least.

The characteristic feature of heavy fermion system can be observed below T_K as listed below.

$T_K < T$ (The impurity Kondo effect behavior)

- The logarithmic temperature dependence of resistivity $\rho(T) \propto -\log T$
- The temperature dependence of χ obeys Curie - Weiss law of $\chi \propto C/(T+\theta)$
- The spin-lattice relaxation rate T_1 shows the behavior of the localized spin system as $1/T_1 = const.$

$T_K < T$ (Kondo singlet and heavy fermion state)

- The temperature dependence of resistivity obeys the T square $\rho(T) \propto T^2$
- The large value of electronic specific heat coefficient γ_{el}
- The susceptibility reach to the constant value
- The spin-lattice relaxation rate T_1 obeys the Koringa law $T_1 T = const.$

1.3 Superconductivity

The investigation of superconductivity has been performed since the discovery of zero resistivity of Hg at 1911 by Kamerlingh-Onnes. When an attractive interaction exists between two electrons, the two electrons can form pairing state in the momentum space near the Fermi surface. Such a electron pair is the so-called "Cooper pair" and it has the properties of Boson particle below T_c. As a result, the Cooper pairs fall into Bose-Einstein condensation, and the superconductivity appears. Bardeen, Cooper and Schrieffer proposed a theory of superconductivity in 1957 [3]. This is a "BCS" theory which can explain the superconducting properties in various metals. The mechanism of the Cooper pairing in the BCS theory is due to electron-phonon interaction. In this situation, the electron-phonon interaction leads isotopic attractive interaction, so that the pairing function (orbital part of the Cooper pair) has isotropic in nature. Namely, an s-wave state realizes. However, the attractive interaction is not always the electron-phonon interaction. Other bosonic interactions, such as spin fluctuation, charge fluctuation, exciton, and etc. can become a pairing interaction[4]. The attractive potential originated in these interactions is anisotropic in nature. Hence, it is expected to realize the anisotropic orbital state of the Cooper pair. In this case, the orbital pairing function has s, p, d, or $f, \cdot\ \cdot$ - wave symmetry,

corresponding to azimuthal quantum number of the electrons pair $L = 0, 1, 2, 3, \cdot\ \cdot$. Such superconductivity is often called as $s, p, d, f, \cdot\ \cdot$ - wave superconductivity, When an electron-phonon interaction is attractive force, the s - wave is realized. On the other hand, anisotropic p, d, f - wave superconductivity has been reported in heavy fermion compounds and high-temperature superconductors. In these system, the anisotropic orbital function would be more suitable to avoid the strong Coulomb repulsion.

1.3.1 Parity of superconductivity

The wave function of superconductivity, which consists of orbital part and spin part, has antisymmetric in nature as for exchange between two electrons, because of the antisymmetric nature of a fermion wave function of a quasiparticle. In general, parity of superconductivity is represented by the parity of orbital part "L". The $s(L = 0), d(L = 2)$ - wave and $p(L = 1), f(L = 3)$ - wave superconductivity are classified as even parity and odd parity, respectively. The spin parts of even and odd parity superconductivity are formed spin singlet S=0 (antisymmetric spin function), and spin triplet S=1 (symmetric spin function), respectively. These superconducting state is described by superconducting order parameter, as mentioned in the next section.

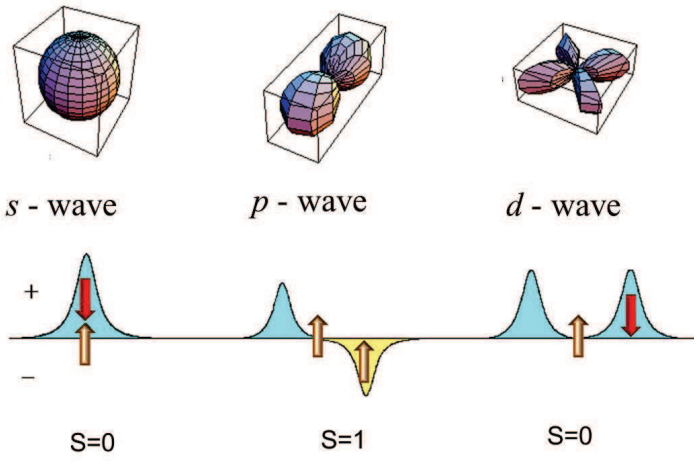


Figure1.2 The wave functions of superconductivity

1.3.2 Superconducting order parameter

The matrix representation of superconducting order parameter can be described as below.

$$\hat{\Delta}(\vec{k}) = \begin{pmatrix} \Delta_{\uparrow\uparrow}(\vec{k}) & \Delta_{\uparrow\downarrow}(\vec{k}) \\ \Delta_{\downarrow\uparrow}(\vec{k}) & \Delta_{\downarrow\downarrow}(\vec{k}) \end{pmatrix} \tag{1}$$

This matrix satisfies the relation of $\hat{\Delta}(\vec{k}) = -{}^t\hat{\Delta}(-\vec{k})$. Here ${}^t\hat{\Delta}(\vec{k})$ is transposed matrix. The total wave function of superconductivity has to be asymmetric because of antisymmetric nature of fermion wave function as mentioned in the previous section. Since the order parameter relates to orbital part, the order parameter has to be symmetric ($\Delta(\vec{k}) = \Delta(-\vec{k})$) in the singlet case ($L$=0,2,4,...) and antisymmetric($\Delta(\vec{k}) = -\Delta(-\vec{k})$) in the triplet case ($L$=1,3,5,...). In the case of singlet superconductivity, the equation (1) has only non-diagonal components as follow.

$$\begin{aligned} \hat{\Delta}(\vec{k}) &= \begin{pmatrix} 0 & \Delta_{\uparrow\downarrow}(\vec{k}) \\ -\Delta_{\downarrow\uparrow}(\vec{k}) & 0 \end{pmatrix} \\ &= \begin{pmatrix} 0 & \Psi(\vec{k}) \\ -\Psi(\vec{k}) & 0 \end{pmatrix} \end{aligned} \tag{2}$$

In the case of triplet superconductivity, the equation (1) can be expressed using three dimensional vector $\mathbf{d}$ as follow.

$$\begin{aligned} \hat{\Delta}(\vec{k}) &= \begin{pmatrix} \Delta_{\uparrow\uparrow}(\vec{k}) & \Delta_{\uparrow\downarrow}(\vec{k}) \\ \Delta_{\uparrow\downarrow}(\vec{k}) & \Delta_{\downarrow\downarrow}(\vec{k}) \end{pmatrix} \\ &= \begin{pmatrix} -\mathrm{d}_x(\vec{k}) + i\mathrm{d}_y(\vec{k}) & \mathrm{d}_z(\vec{k}) \\ \mathrm{d}_z(\vec{k}) & \mathrm{d}_x(\vec{k}) + i\mathrm{d}_y(\vec{k}) \end{pmatrix} \end{aligned} \tag{3}$$

Here, d-vector is defined as

$$\Delta_{\uparrow\uparrow}|\uparrow\uparrow\rangle + \Delta_{\uparrow\downarrow}\left(|\uparrow\downarrow\rangle + |\downarrow\uparrow\rangle\right) + \Delta_{\downarrow\downarrow}|\downarrow\downarrow\rangle = d_x|x\rangle + d_y|y\rangle + d_z|z\rangle. \tag{4}$$

The left side of equation of (4) expresses the order parameters by basis of spin state $|\uparrow\uparrow\rangle$, $\frac{1}{\sqrt{2}}(|\uparrow\downarrow\rangle + |\downarrow\uparrow\rangle)$ and $|\downarrow\downarrow\rangle$. The basis of right side of equation of (4) is expressed as follow.

$$|x\rangle = \frac{1}{\sqrt{2}}\left(-|\uparrow\uparrow\rangle + |\downarrow\downarrow\rangle\right)$$

$$|y\rangle = i\frac{1}{\sqrt{2}}\left(|\uparrow\uparrow\rangle + |\downarrow\downarrow\rangle\right) \tag{5}$$
$$|z\rangle = \frac{1}{\sqrt{2}}\left(|\uparrow\downarrow\rangle + |\downarrow\uparrow\rangle\right)$$

The z - axis of basis of d - vector is perpendicular to quantization axis of spin. In the case of the spin triplet superconductivity, the degree of freedom attributed to spin remains and can be expressed by d - vector.

2 Introduction

2.1 Crystal structure

UBe_{13} is one of the most exotic heavy fermion superconductor, which was discovered by Ott *et al.*, in 1983 [1]. This compound shows superconducting transition at $T_c = 0.86$ K. The physical properties in normal and superconducting states are pretty different from other heavy fermion compounds. UBe_{13} crystallizes in the cubic $NaZn_{13}$-type structure with space group O_h^6(No.226, Fm $\overline{3}c$) as shown in figure 2.1. The lattice constant is a=10.257 Å. In the crystallography, the Be atoms have two different site. Be(I) atoms occupy the 8b site with cubic symmetry of ($m\overline{3}$.) and Be(II) atoms occupy the 96g with orthorhombic symmetry (m..). Each Be(I) are surrounded by twelve Be(II) atoms which form irregular icosahedral cage. From a different viewpoint, each U is surrounded by twenty-four Be(II) atoms which form snub-cube as shown in figure 2.2.

Table1 The representative atomic sites of U, Be(I) and Be(II) in UBe_{13}. Here, y and z are $y = 0.1761$ and $z = 0.1141$.

Atom	Occupancy	Wyckoff Site	Site symmetry	x	y	z
U	8	a	432	1/4	1/4	1/4
Be(I)	8	b	$m\overline{3}$.	0	0	0
Be(II)	96	i	m..	0	y	z

2.2 Unusual physical properties in the normal state

Figure 2.3 shows the temperature dependence of the specific heat reported by Ott *et al.* in 1986[1]. The electronic specific heat coefficient is extremely large ($\sim$ 1100mJ/mol K^2) associated with strong electronic correlations. The superconducting transition occurs at T_c with a large specific heat jump, indicating that the heavy quasi particles are responsible for superconductivity.

Figure2.4 shows the temperature dependence of the resistivity [5, 6]. The resistivity increases with decreasing temperature from room temperature and its temperature

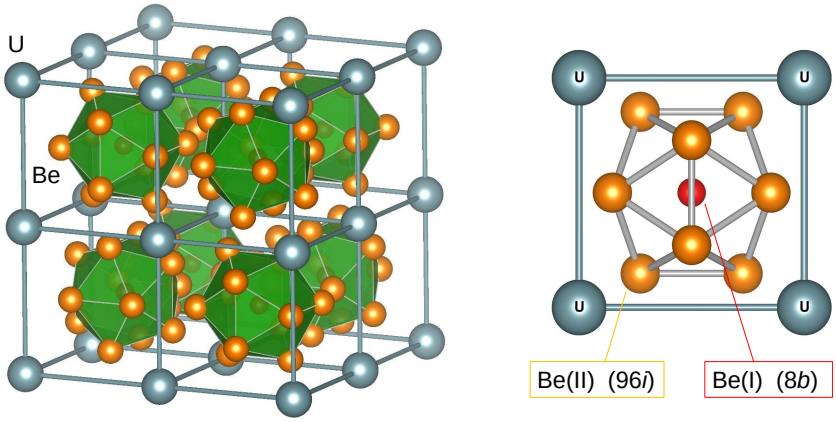


Figure2.1 The crystal structure of UBe_{13}

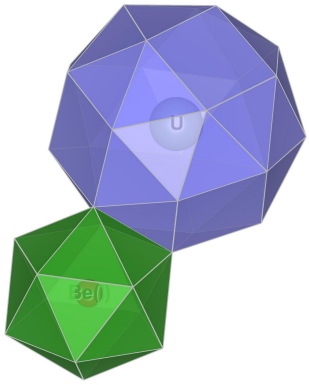


Figure2.2 The cage structure which are consisted by Be(II) atoms around U atom and Be(I) atom.

dependence follows as $\rho \propto -\ln T$. Such a logarithmic temperature dependence of resistivity is attributed to the Kondo effect associated with the exchange interaction between conduction electrons and localized U $5f$ electrons. At high temperature region, magnetic susceptibility follows the Curie-Weiss law, indicating that $5f$ electrons of U is localized. The resistivity reaches constant value around 20 K and stays almost constant in the temperature range between 20-5 K. Below 5K, the resistivity shows a broad peak around 2 K. The general behavior of $\rho \propto T^2$ expected in a typical

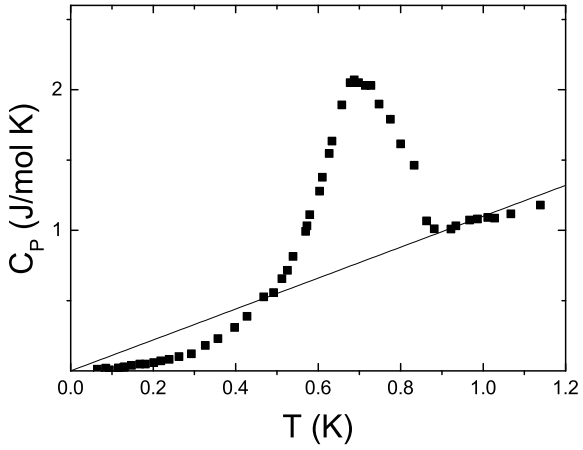


Figure2.3 The temperature dependence of the specific heat in UBe_{13}. (The original data have been reported in [1].)

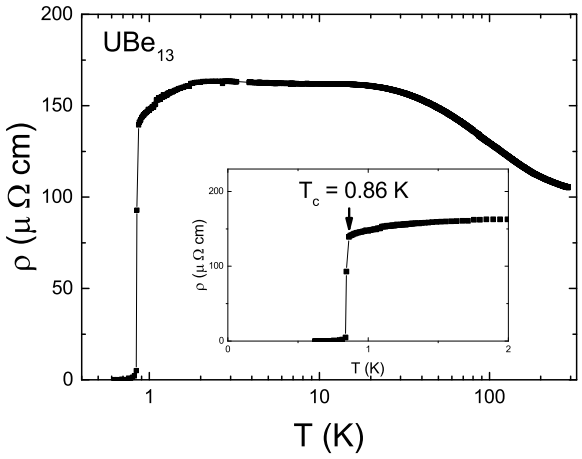


Figure2.4 Temperature dependence of resitivity. (The original data have been reported in [5, 6].)

heavy fermion system cannot be observed down to the superconducting transition at 0.86 K in UBe_{13}. At low temperatures below 10 K, magnetic susceptibility diverges with decreasing temperature. These unusual physical properties are reminiscent of a non-Fermi liquid behavior. Although many theoretical works to elucidate the unusual physical properties of UBe_{13} have been done so far, a consensus has not been reached

yet.

2.3 Unconventional superconductivity

2.3.1 Superconducting gap

In the early stage, temperature dependences of specific heat, C/T[1, 7], NMR spin-lattice relaxation rate, $1/T_1$[8], and ultrasound attenuation[9] etc. show power-low of T^n in the superconducting state, suggesting the existence of nodal superconducting gaps. Recently, however, Shimizu and coworkers carried out angle-resolved specific-heat measurements and demonstrated that the magnetic-field dependence of $C(H)$ is proportional to H with no angular dependence at low fields in the superconducting state. Furthermore, they pointed out that the temperature dependence of $C(T)$ can be well explained by a three band full-gap superconducting state. Thus, the superconducting gap is fully open over the Fermi surfaces in contrast to the early works[10].

2.3.2 Superconducting upper critical field $H_{c2}(T)$

The superconducting upper critical field $H_{c2}(T)$ exhibits unusual upward curve. $H_{c2}(0) \approx 10 \sim 12$T depending on the sample. The upper critical field field exceeds the Pauli limiting field $H_p \approx 1.6$ T.

The initial slope of $H_{c2}(T)$, $-(dH_{c2}/Td)_{T\to T_c}$ is quite large, $-(dH_{c2}/Td)_{T\to T_c} \approx 26 \sim 200$ T/K depending on estimations[1, 11]. Thus the upper critical field is estimated to be $H_{c2}(0) \approx 21 \sim 160$ T. However, these values are quite large compared to the observed upper critical field, $H_{c2}(0) \approx 10 \sim 12$T, suggesting the Pauli paramagnetic effect[12]. In any case, unusual upward curvature of $H_{c2}(T)$ cannot be understood in the framework of the conventional BCS theory[13, 14, 15].

2.3.3 Anomaly in the superconducting state

In addition to the unusual superconducting upper critical field, the superconducting phase diagram of UBe_{13} is quite unique in comparison with other Heavy Fermion superconductors. Various thermodynamic transport measurements, such as specific heat[16, 17, 18, 19], dc magnetization[20], surface impedance measurements[21] shows anomalous behavior inside in the superconducting phase. The anomalies are observed

at B^* and the $H-T$ phase diagrams are summarized in figure 2.5 and figure 2.6. Similar superconducting phase diagram was reported for UPt_3 [22], where multiple superconducting phase diagram in UPt_3 is attributed to a degenerated superconducting order parameter inherent in a spin-triplet superconducting state. In the early stage, a possibility of the spin-triplet superconductivity having a degenerated order parameter has been discussed in UB_{13} on the analogy of UPt_3. However, recent dc-magnetization measurements by Shimizu and co-workers revealed that such anomalies are not ascribed to the degenerated superconducting order parameter but rather to either unusual superconducting diamagnetic response or short-range ferromagnetic order in the vortices.

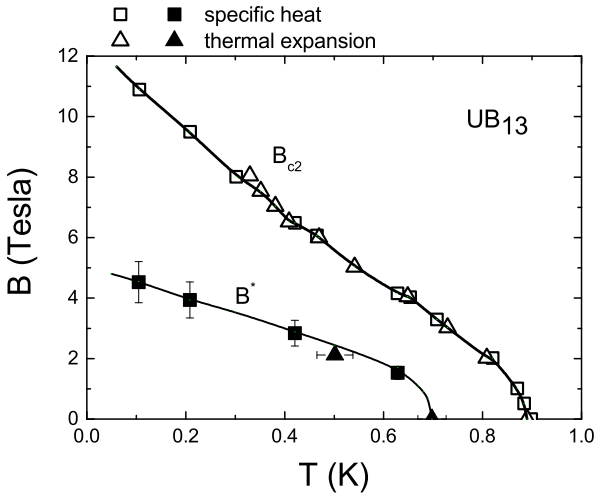


Figure2.5 $T-H$ SC phase diagram from specific heat. (The original data have been reported in [23].)

2.3.4 NMR and μSR

In the early stage before millennium, NMR studies on UBe_{13} and Th-doped UBe_{13} were reported by MacLaughlin's group[8, 24, 25, 26]. Tien and Jiang reported the results of temperature dependence of the ^{9}Be-Knight shift for polycrystal sample which shows no change on passing through T_c and suggested that a spin triplet superconducting state is realized in UBe_{13}[25]. On the other hand, μSR Knight shift measurements demonstrated that the μ^+-Knight shift decreases below T_c by about 40

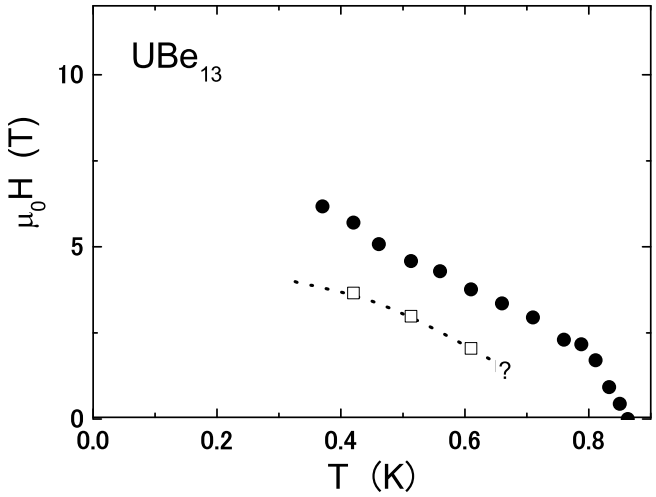


Figure2.6 $T-H$ SC diagram from surface impedance. (The original data have been reported in [21].)

% against the normal state value of the spin susceptibility [27]. They claimed that the pairing state is either an even parity spin-singlet state or an odd-parity spin-triplet state with strong spin-orbit coupling for the Cooper pairs.

Recently, a high quality single crystals have been synthesized by Haga *et al.*(JAEA) and NMR studies have been carried out by Tou's group[2, 28]. In the normal state, Morita *et al.* reported temperature dependence of NMR spectra and nuclear spin-lattice relaxation rate under various fields for the field parallel to [111] direction in the temperature range between room temperature and 1.5 K. They suggested that the ground state is a non-magnetic crystal electric field (CEF) state and the CEF gap between the ground and the 1st excited states is about 100 K. In the superconducting state, NMR Knight shift measurements have been performed under various fields for the applied field parallel to [001], [110] and [111] directions in the temperature range between 1 K and 0.4 K. ^{9}Be-NMR Knight shift shows no change on passing through T_c down to T_a at which the anomalies are detected by many thermodynamics, as mentioned before. Simply, this result suggests that the superconductivity of UBe_{13} is a spin-triplet pairing state. However, they reported that the anomalies in NMR Knight shift is observed for the magnetic field parallel to [001] and [011] directions,

whereas the shift for the field parallel to [111] increases below T_a. As for experimental condition, observed temperature range of $0.4 - 1$ K is not sufficient to discuss the superconducting order parameter. Furthermore, such complex NMR results cannot be understood by simple models. Therefore, further detailed NMR studies are required.

3 Purpose

The purpose of the present study is to clarify the nature of the superconducting state in UBe_{13} by NMR and surface impedance measurements.

Especially, two open questions are remained to be clarified as listed below.

- Parity of the superconducting state
- Origin of the anomaly at T_a or B^*

The previous NMR results using a high quality single crystal suggested that a spin-triplet superconductivity is realized in UBe_{13}. However, the NMR measurements have not been performed below 0.4 K, which is about one half of T_c. The temperature range is not sufficient to extract the intrinsic superconducting properties. Furthermore, complicated NMR data depending on magnetic field-strengths and field-directions for the crystal axis, which would be reminiscent of the origin of the anomaly in the superconducting phase diagram, prevent us to gain comprehensive NMR results. At the present stage, NMR data are still fragmentary to discuss the superconducting state in UBe_{13}. Thus, further detailed NMR data for various field-strengths, field-directions, and low temperatures below 0.4 K, and their careful data analyses are required to understand the unconventional superconducting state in UBe_{13}.

In this study, we have carried out the measurements of detailed ^{9}Be-Knight shift under various magnetic fields and field-directions at low temperatures down to below 0.05 K to gain elementary excitations inherent in the unconventional superconducting state in UBe_{13}. Furthermore, in order to clarify the origin of the anomaly observed in the superconducting state, surface impedance measurements have been carried out below 0.1 K using dilution refrigerator.

4 Experimental procedure

4.1 Sample

The sample used in this studies was provided by Haga *et al.* (JAEA). It was synthesized by Al-flux method. The dimension of the single crystal of UBe_{13} is $L([110]) \times W([1\bar{1}0]) \times H([001]) \sim 1.7\text{mm} \times 1.8\text{mm} \times 2.0\text{mm}$ as shown in figure 4.1. Figure 4.1(a) shows the picture of the sample and (b) shows a sketch of crystal [5].

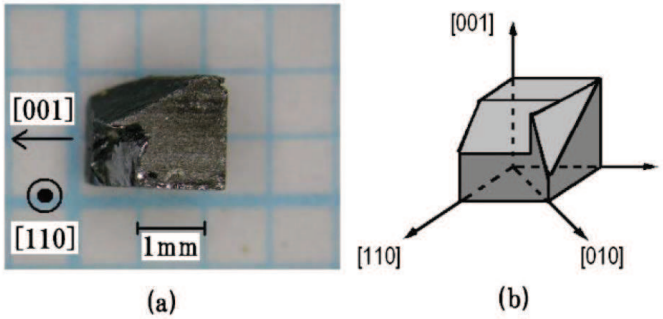


Figure4.1 (a)The single crystal sample of UBe_{13} (b)The crystal axis

4.2 Apparatuses

4.2.1 NMR apparatus

Nuclear Magnetic Resonance (NMR) measurements were carried out by the Hahn spin-echo technique using a phase coherent type NMR spectrometer. The schematic block diagram of an NMR system is shown in figure 4.2. Radio frequency (RF) continuous wave with characteristic frequency ω_0 generated by a signal generator and periodic pulse sequences, in which the characteristic width of a pulse is Δt, generated by a pulse generator are mixed in the RF switch. The RF pulses generated like this are enhanced by an RF power amplifier. Then the amped RF pulses are applied to the sample through an NMR probe that consists of a coil and capacitors forming an LC resonance circuit. Here, ω_0 is determined so as to satisfy the resonance condition of $\omega_0 = 1/\sqrt{LC}$. Nuclear spins in the sample are excited by the RF magnetic field,

$H_1 \cos \omega_0 t$, where H_1 is determined so as to satisfy the relation of $\gamma H_1 \Delta t = \pi/2$ or π. The RF resonance circuit is also utilized to detect the nuclear magnetization in the sample using the Faraday electromagnetic induction due to the precession of nuclear moments. Since the obtained NMR signals are small as less than about nV$\sim \mu$V, the signals are amped by a receiver. For amped signals, the RF component is subtracted in a phase sensitive detector. Then obtained NMR signals have audible frequency range and are further enhanced by an audio amplifier. Furthermore, the obtained analog NMR signals are converted through an A-D conversion. Thus obtained NMR signals are integrated and analyzed by a computer.

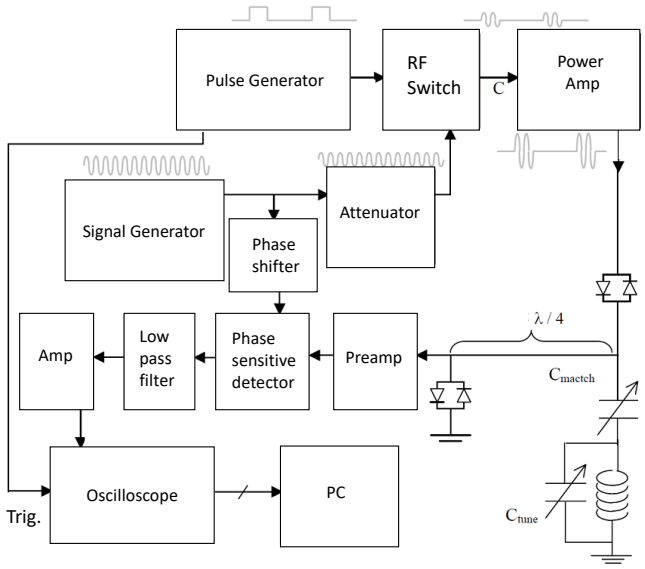


Figure4.2 The picture of concept of measuring device

4.2.2 Superconducting magnets

To apply the external magnetic field, solenoid type superconducting magnets were used as shown in figure 4.3 and 4.4. These magnets can generate magnetic field up to 8 T (Oxford), 12 T(Cryogenic), and 17 T (Oxford) with their field-homogeneity of $\sim 10^{-3}$/10mmDSV, where DSV means diameter spherical volume.

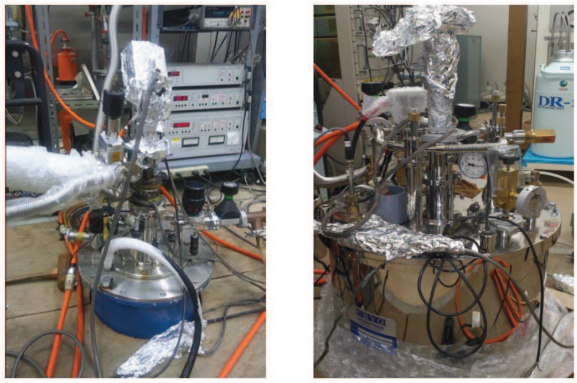


Figure4.3 The picture of SC magnets (a)8 T SC magnet (b)12 T magnet

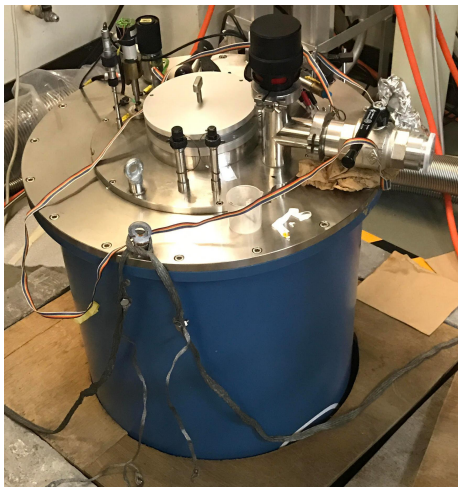


Figure4.4 The picture of SC 17 T magnet

4.2.3 Cryostats

Our NMR measurements were carried out in the temperature range of 0.03-300 K. Above 1.5 K, we used VTI(Variable Temperature Insert) and the sample was settled in the vaporized helium gas or evacuated liquid helium. Below 1.5 K, we use three kinds of cryostats, a closed cycle home-made ^{3}He refrigerator (figure 4.5), a SAAN ^{3}He-^{4}He-dilution refrigerators (figure 4.6) and a Oxford ^{3}He-^{4}He-dilution refrigerator (figure 4.7). In the temperature range of 1.5 $\sim$ 0.4 K, we used the ^{3}He refrigerator. In the temperature range of 1 $\sim$ 0.05 K, ^{3}He-^{4}He-dilution refrigerators were used.

Especially, a uniaxial goniometer is attached to the mixing chamber of the Oxford dilution refrigerator, field-angle dependence of NMR measurements were carried out this Oxford ^{3}He-^{4}He-dilution refrigerators (figure 4.7).

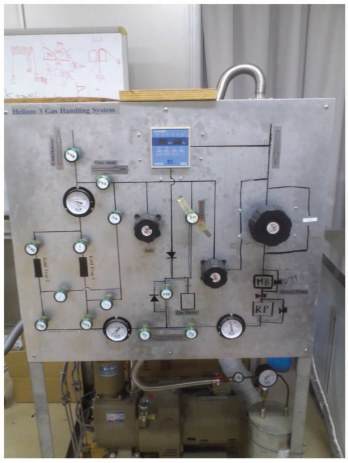


Figure4.5 ^{3}He refrigerator



Figure4.6 Dilution refrigerator



Figure4.7 Dilution refrigerator(Oxford)

5 Introduction to NMR and Surface Impedance

5.1 Hyperfine interaction and nuclear quadrupole interaction

The NMR measurements can obtain the information of the local electronic state for interesting nucleus from the microscopic view point. The NMR parameters mostly depend on the local atomic configurations, such as electronic and magnetic states of ligand ions, and electron density of states at Fermi level, via hyperfine and nuclear quadrupole interactions. In this section, we summarize the principles of NMR.

The effective Hamiltonian of nuclear spin can be described as below.

$$\mathcal{H} = \mathcal{H}_Z + \mathcal{H}_Q + \mathcal{H}_{hf} \tag{6}$$

The first term is the Zeeman interaction between nuclear spin moment $\boldsymbol{\mu}_n = \gamma_n \hbar \boldsymbol{I}$($\boldsymbol{\gamma}_n$:nuclear gyromagnetic ratio) and magnetic field $\boldsymbol{H}_0$;

$$\mathcal{H}_Z = -\gamma_n \hbar \boldsymbol{I} \cdot \boldsymbol{H}_0 \tag{7}$$

The second term is the nuclear quadrupole interaction which relates to a nuclear quadrupole moment and the electric field gradient (EFG) due to non-spherical distribution of the electron charge (orbit). When $I \geq 1$, the nucleus has an electric quadrupole moments eQ ($Q = \int_V (3z^2 - r^2) dv$). In this situation, the nuclear quadrupole interaction is effective and the eigen energy levels of the nucleus spin are split into several doublets. The electric quadrupole Hamiltonian can be described as below,

$$\begin{aligned} \mathcal{H}_Q &= \frac{e^2 qQ}{4I(2I-1)} \left\{ (3I_z^2 - I^2) + \frac{1}{2}\eta (I_+^2 + I_-^2) \right\} \\ &= \frac{1}{6} h\nu_Q \left\{ (3I_z^2 - I^2) + \frac{1}{2}\eta (I_+^2 + I_-^2) \right\}. \end{aligned} \tag{8}$$

Here, ν_Q is the so-called quadrupole frequency, eq the electric field gradient, and η the asymmetry parameter, which are defined as,

$$\nu_Q = \frac{3e^2 qQ}{2hI(2I-1)}, \quad eq \equiv V_{zz}, \quad \eta \equiv \frac{V_{xx} - V_{yy}}{V_{zz}}. \tag{9}$$

These parameters are related with electrostatic potential V and $V_{\alpha\beta} (\alpha, \beta = x, y, z)$ is defined as the second derivatives of V, i.e., $V_{\alpha\beta} = \partial V / \partial\alpha \partial\beta$.

The last term is a hyperfine interaction between nuclear spin and surrounding electrons. This Hamiltonian can be described by

$$\mathcal{H}_{hf} = \gamma_e \gamma_n \hbar^2 \left[\frac{8\pi}{3} \delta(r) \boldsymbol{I} \cdot \boldsymbol{S} - \left(\frac{\boldsymbol{I} \cdot \boldsymbol{S}}{r^3} - \frac{3(\boldsymbol{I} \cdot \boldsymbol{r})(\boldsymbol{S} \cdot \boldsymbol{r})}{r^5} \right) + \frac{\boldsymbol{I} \cdot \boldsymbol{l}}{r^3} \right]. \tag{10}$$

Here, $\boldsymbol{S}$, $\boldsymbol{l}$, and γ_e are the total electron spin ($\boldsymbol{S} = \sum s$) and orbital angular momentum of electrons, and electron gyromagnetic ratio, respectively.

The first term of this Hamiltonian is called as "Fermi contact hyperfine". This interaction is caused by s-electrons which has finite possibility at the nuclear position. The second term is spin-dipolar interaction caused by onsite non s-electrons, i.e., p, d, f-electrons. The last term is the interaction between the nuclear spin and orbital current of non s-electron. Furthermore, we have indirect interaction between nuclear spin and onsite non-s-electron spins expressed by

$$\mathcal{H}_{hf}^{indirect} = \frac{8\pi}{3} \gamma_e \gamma_n \hbar^2 \sum_i \left(|\Psi_i(0)^{\uparrow}|^2 - |\Psi_i(0)^{\downarrow}|^2 \right) \boldsymbol{I} \cdot \boldsymbol{S}, \tag{11}$$

where $|\Psi_i(0)^{\uparrow}|^2$ is the probability density of closed s-electrons. This interaction is the indirect interaction due to core polarization effect where the closed inner s-electrons are polarized by unpaired p, d, f-electrons through the exchange interaction.

5.1.1 NMR spectrum

Observed NMR line profile changes owing to the strength of the relation between the Zeeman interaction and nuclear quadrupole interaction. Figure 5.1 displays the energy splitting for nuclear spin level and expected NMR line profile. The left hand-side shows when only the Zeeman interaction exists, while the right hand-side indicates when the Zeeman interaction with a weak quadrupole interaction as a perturbation for $\mathcal{H}_z \gg \mathcal{H}_Q$ where η=0.

When the principal axes of the quadrupole interaction does not coincide with those of Zeeman interaction, equation (9) is rewritten as follows.

$$\begin{aligned} \mathcal{H}_Q = \frac{e^2 qQ}{4I(2I-1)} \big[& \frac{1}{2} \left(3\cos^2\theta - 1 \right) \left\{ 3I_z^2 - I\left(I+1\right) \right\} \\ & + \frac{3}{2} \sin\theta\cos\theta \times \left\{ I_z \left(I_+ + I_- \right) + \left(I_+ + I_- \right) I_z \right\} \\ & + \frac{3}{4} \sin^2\theta \left(I_+^2 + I_-^2 \right) \big] \end{aligned} \tag{12}$$

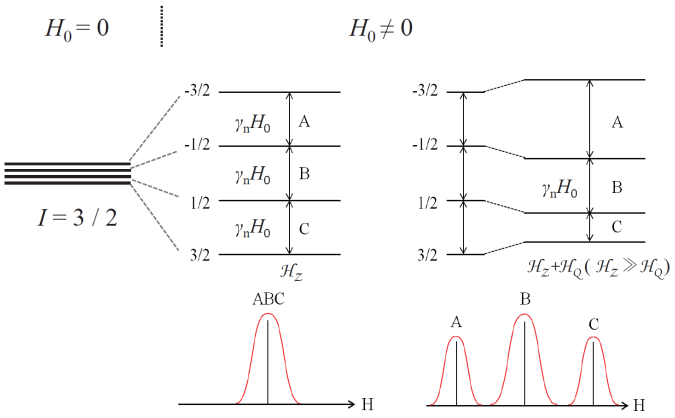


Figure5.1 The Energy levels and obserble spectra in the case of $I = 3/2$

Here we assume axial symmetry of the quadrupole interaction, i.e. $\eta = 0$ for simplicity. θ is the polar angle of EFG principal axis with respect to the principal axis of applied field $\boldsymbol{H}_0$, as shown in the Figure 5.2. As we can see the Equation (13), the Hamiltonian depends on the field angle θ, so that the NMR line profile as well as the energy splitting due to the quadrupole interaction shown in the Fig.5.1 depends on θ.

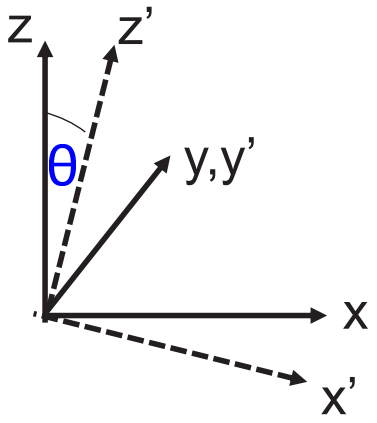


Figure5.2 The principal axes of the applied field are represented by x, y, and z. Those of the EFG are expressed as x', y', z'. The polar angle θ of the direction of the maximum principal axis of the EFG is defined with respect to the z -direction of the magnetic field.

5.1.2 Knight shift and local field

In general, the nucleus is affected by the internal local field $\boldsymbol{H}_{\rm loc}$ which is produced by surrounding electrons. The local field is not always static, so that it can be divided into static and fluctuating components and described below.

$$\boldsymbol{H}_{\rm loc}(t) \;=\; \langle \boldsymbol{H}_{\rm loc} \rangle + \delta \boldsymbol{H}(t) \tag{13}$$

Here, $\langle \boldsymbol{H}_{\rm loc} \rangle$ means the average value of the internal field, i.e., static contribution, and $\delta \boldsymbol{H}(t)$ means time dependent term of the internal field, fluctuating contribution. $\delta \boldsymbol{H}(t)$ contributes to the relaxation process of nuclear spin related to the energy dissipation between the nuclear spin and other surroundings. On the other hand, $\langle \boldsymbol{H}_{\rm loc} \rangle$ causes NMR line shift via hyperfine interactions as mentioned in the previous section. Such an NMR line shift caused by surrounding electrons is called as "Knight shift". The Knight shift is defined as follows.

$$K = \frac{H_{loc}}{H_0} \tag{14}$$

A schematic sketch of the effect of Knight shift to the NMR line is shown in Fig.5.3.

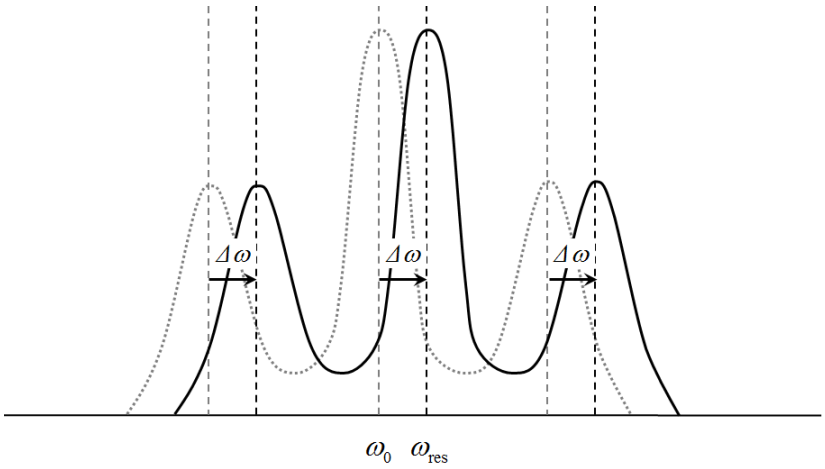


Figure5.3 NMR shift of the resonance line due to the hyperfine interaction.

5.2 Surface impedance measurements

5.2.1 Theoretical back ground

In order to understand the nature of the unconventional superconductivity, it is important to detect low-energy excitation of quasiparticles in the superconducting state. This is because such low-energy excitations are related to the unconventional pairing mechanism. It is well known that specific heat, thermal conductivity and NMR measurements, etc. are effective tools. In addition, surface impedance measurement also provides useful information on the quasiparticle excitations. In this section, we describe the surface impedance measurement in the radio-frequency range, namely, RF surface impedance method.

In general, the electromagnetic response of a metallic material is described by a complex surface impedance as

$$Z_{=}R_s + iX_s, \tag{15}$$

where R_s is the surface resistance, and X_s is the surface reactance. This equation is a consequence of the dissipation and energy stored inside the metallic material.

In the highly conductive material, classical electromagnetism tells us the skin-depth effect that an applied electromagnetic field decays with a characteristic length, the so-called "skin depth", δ.

Firstly, we consider the case that the Ohm's law of "$\boldsymbol{i} = \sigma \boldsymbol{E}$" is completed for the surface region, i.e., local limit. When the electromagnetic field is applied to the surface of the metallic material, the electric field perpendicular to the surface is damped as,

$$E_x(z) = E_x(0)e^{-(1+i)z/\delta}, \tag{16}$$

where we define this direction as z. δ is the skin-depth and is expressed as,

$$\delta = \sqrt{\frac{2}{\omega\mu\sigma_1}}, \tag{17}$$

where the μ is the permeability. The damping along the z direction, i.e., z-derivative, is much stronger than those along x or y-directions, i.e., x- or y-derivative. Therefore, the electromagnetic field in the material is tangential to the surface, i.e., E_x and H_y or E_y and H_x, where $H \perp E$ is a consequence of the classical electromagnetism.

Furthermore, the relation between the electric field and the magnetic field is expressed as

$$H_y(z) = \frac{1-i}{\mu_0 \omega \delta} E_x(z). \tag{18}$$

Then, surface impedance is expressed as,

$$Z = \frac{E_x}{\int_0^\infty i_x(z)dz} = \left.\frac{E_x(0)}{H_y(0)}\right|_{z=0} = i\omega\mu_0 \left.\frac{E_x(0)}{\frac{\partial E_x(z)}{\partial z}}\right|_{z=0} \tag{19}$$

Using the Eqs.(18) and (19), we have

$$Z = \frac{1+i}{2}\mu_0\omega\delta = (1+i)\left(\frac{i\omega\mu_0}{2\sigma}\right)^{1/2}. \tag{20}$$

The local limit is not always completed for metallic materials. When the skin depth is shorter than the mean free path, l, of conduction electrons, the electric field is not constant in the surface area. Therefore, the local limit is violated, $\boldsymbol{i} \neq \sigma \boldsymbol{E}$. In this case, the current i is not uniform and the electric field over a volume limited to l. In this case, the surface impedance is connected to the inverse of complex conductivity $\tilde{\sigma} = \sigma_1 - i\sigma_2$ and is given by

$$Z_s = \left(\frac{i\omega\mu_0}{\tilde{\sigma}}\right)^{1/2}, \tag{21}$$

where ω is the angular frequency, and μ_0 is the permeability of vacuum.

Thus, the conductivity σ of the sample is a crucial key factor for surface impedance measurements. Experimentally, as for the RF surface impedance measurement, the energy loss of the electromagnetic field, $\Delta\langle W\rangle$, is involved with the changes of the resonance frequency and quality factor Q of the LC circuit as

$$\frac{\langle \Delta W\rangle}{\langle W\rangle} = \frac{\Delta f}{f_0} - \frac{i}{2}\Delta\left(\frac{1}{Q}\right). \tag{22}$$

where $\langle W\rangle$ is the electromagnetic energy stored in the coil. In highly conductive metals, the conductivity is sufficiently high then we can set $\mu \approx \mu_0$. Therefore $\langle \Delta W\rangle/\langle W\rangle$ is in proportion to Z_s.

5.2.2 RF surface impedance measurement

In this study, RF frequency wave is utilized to obtain the Z_s of the single crystal UBe_{13}. The residual resistivity ρ_0 of UBe_{13} is about $\rho_0 \approx 130\mu\Omega$cm. Due to the

skin-depth effect, electromagnetic field can penetrate to δ, which is much longer than the mean free path l as

$$\delta_n \gg l. \tag{23}$$

From the Eqs. (15) and (22), R_s and X_s are expressed as

$$R_s = A(R_s' - R_0'), \tag{24}$$
$$X_s = G(f_0 - f_s)/f_0 + C, \tag{25}$$

where R_s' and R_0' are the surface resistances at the resonance condition with and without the sample, respectively. f_0 and f_s are the resonance frequencies of the circuit with and without the sample, respectively. The resonance frequency is expressed as

$$f = \frac{1}{2\pi\sqrt{LC}}. \tag{26}$$

A and G are the geometrical factors, and C the metallic constant. The surface resistance R' is extracted from the return loss (r) of the LC circuit. The return loss is expressed with amplitude of incident and reflected wave (V_0,V) as follows.

$$r = -20\log\left|\frac{V}{V_0}\right| \tag{27}$$

This can be rewritten with impedance of circuit as,

$$-20\log\left|\frac{V}{V_0}\right| = -20\log\frac{|Z - Z_0|}{Z + Z_0}, \tag{28}$$

where, Z_0 is characteristic impedance of circuit, about 50Ω. In the resonance point, the equation (26) is satisfied and reactance become zero. Therefore, we have the following relation as

$$X = L\omega - \frac{1}{\omega C} = 0. \tag{29}$$

Thus, the impedance can be expressed as below.

$$Z \cong R. \tag{30}$$

From the equation (28), the resistance of circuit R' is determined by the relation

$$R' = Z_0\frac{10^{r/20} \pm 1}{1 - 10^{r/20}}. \tag{31}$$

The observed frequency f (equation(26)) and the return loss (equation (28)) include the background impedance from the surrounding metallic coil and sample holder. To sabstruct the background, we measured the surface impedance of the LC circuit itself.

In a normal metallic state, the surface resistance and surface reactance can be expressed as

$$Rs = Xs = \frac{1}{2}\mu_0\omega\delta_n. \tag{32}$$

In a superconducting state, the resistivity and reactance can be expressed as

$$Rs \cong 0, Xs \cong \mu_0\omega\lambda. \tag{33}$$

Here, the λ is field penetration depth.

5.2.3 Surface impedance in the superconducting state

In the type II superconductor, a vortex state is realized between H_{c1} and H_{c2}. In this case, the superconducting state is partially broken and quantized vortices penetrate inside in the superconductor. Generally, these vortices form the triangle lattice to minimize the repulsion, where the superconducting state is broken and quasiparticles are excited around the vortices within the coherence length, ξ.

When we apply an RF field H_ω perpendicular to the vortex (Fig.5.4), then current ($\boldsymbol{J}$) flows to shield the RF field penetration into the superconductor. Then vortices receive the Lorentz forces, $\boldsymbol{f}_L = \boldsymbol{J} \times \boldsymbol{B}$ and cause to move. The motion of vortexes give rise to an finite electrical resistivity, the so-called "flux-flow resistivity" ρ_f, in the superconducting state.

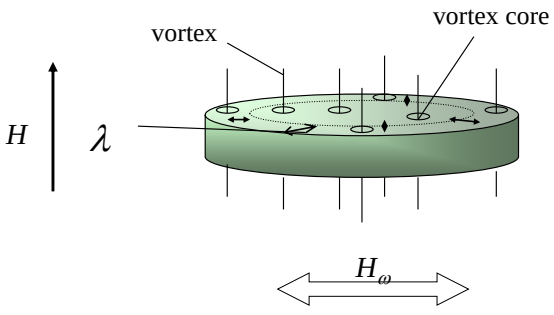


Figure5.4 vortex lattice

Since the normal core increase with increasing of the external magnetic field, ρ_f increases with increasing field. As for an s- wave superconductor, the field dependence

of ρ_f can be expressed with resistivity of normal state ρ_n as below[29].

$$\rho_f(H) = \rho_n \frac{H}{H_{c2}} \tag{34}$$

On the other hand for the anisotropic superconductor, such as high-T_c cuprates, heavy fermion system and so on, ρ_f show differenct behavoir as follow[30].

$$\rho_f(H) \propto \sqrt{\frac{H}{H_{c2}}} \tag{35}$$

5.2.4 Pinning effect

The impurities and/or defects can pin the motion of the vortices. This effect is called the pinning effect. The zero resistance sate is maintained as long as Lorentz force exceeds the pinning potential. At high temperatures, the vortex can move to neighbor site by thermal effect via hopping. Figure 5.5 displays schematic sketch of the relationship between the vortex hopping and the pinning potential. Figure 5.5 (a) shows the vortex pinning state trapped by impurity potential U. In this case, nothing occurs. (b) When a weak electromagnetic field is applied to the sample, a Lorentz force due to the shielding current is active and the pinning potential is deformed and the hopping form a potential to another potential occurs. (c) When a strong electromagnetic field is applied, the Lorentz force exceeds the potential barrier. Then, the vortex can move freely. This state is the so-called as the free-flux flow state.

In the low frequency measurements, the Lorenz force is not enough strong to exceed the pinning potential. Hence, the flux flow resistivity is suppressed and it becomes large with increasing the frequency.

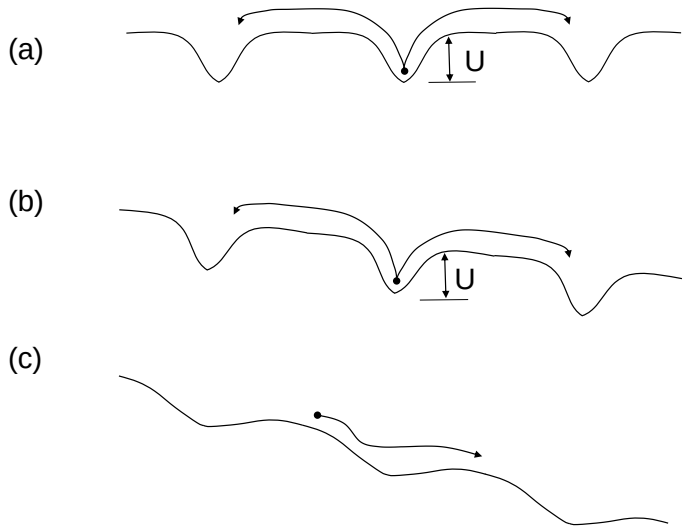


Figure5.5 The schematic of pinning potential (a)The case of no electric field (b)the case of the weak Lorenz force (c)the case of Lorenz force defeats pinning

6 Result

6.1 Surface impedance

The RF surface impedance measurements have been carried out at three frequencies (6.3, 71, 97 MHz) for the applied field parallel to [111] direction.

Temperature dependence of $(f_0-f_s)/f_0$ can be scaled to R_s-R_0 in the normal state, and both are agree well with the square root of the electrical resistivity[21]. Therefore, the Hargen-Rubens relation of $R_s = X_s = \mu\omega\delta_n/2$ is maintained at least below 5 K. In this case Drude complex conductivity $\sigma(\omega)$ is approximately expressed as $\sigma(\omega) = \sigma_0/(1+i\omega\tau) \approx \sigma_0$, where σ_0 and τ are the frequency-independent conductivity, and the scattering relaxation time of quasiparticles, respectively. At the observed frequencies of 6.3, 71, and 97 MHz, temperature dependence of $(f_0 - f_s)/f_0$ is scaled to $R_s - R_0$ in the normal state, so that we confirm that the Hargen-Rubens relation is utilized for the present data.

Figure 6.1 displays the magnetic field dependences of the surface resistance R_s and the surface reactance X_s measured at several temperatures, 0.3 K, 0.2 K, and 0.1 K in the magnetic field range of 0−10 T. Figure 6.2 shows the data of 6.3 MHz together with the previous data measured at 5.7 MHz[21]. Figure 6.3 displays R_s and X_s measured at 71 MHz for several temperatures, 0.7 K, 0.5 K, 0.4 K, 0.3 K, 0.2 K, and 0.1 K. The data are scattered because of weak return loss signals because we measured at the resonance frequency for higher harmonic frequency. Figure 6.4 displays R_s and X_s measured at 97 MHz for several temperatures, 0.6 K, 0.5, K, 0.2 K, and 0.1 K.

Firstly, we mention the properties of normal state. We found that both R_s and X_s decreases with increasing magnetic field. The suppression of the resistivity by the magnetic field, i.e., negative magnetoresistance, is commonly observed in most heavy fermion materials. The negative magnetoresistance is understood by the breakdown of the Kondo singlet due to the magnetic field. In fact, the temperature dependence of $\rho(T)$ of UBe_{13} exhibits logarithmic divergence with decreasing temperature, evidencing that the Kondo effect works. This behavior tells us the Kondo temperature T_K as less than 5 K, using the relation of $\mu_B H_K \approx k_B T_K$. In addition, both R_s and X_s at 0.1 K is suppressed much more than those at higher temperatures. These

tendencies are more clear at high frequency.

Next, we focus on the behavior in the superconducting state. At low frequency, $f = 5 \sim 6.3$ MHz, $R_s(H)$ and $X_s(H)$ are suppressed significantly above $H^* \approx 0.4H_{c2} - 0.6H_{c2}$ with increasing H. These features are quite different from conventional s-wave superconductors [31]. In general for some unconventional superconductors, vortex pinning due to impurities, defects, and stacking faults in the crystal lattice is observed near H_{c2} ($H_p \approx 0.9H_{c2}$). [6] Furthermore an inhomogeneous superconducting state of the Fulde-Ferrell-Larkin-Ovchinnikov state also causes such a vortex pinning. However, the observed anomaly, $H^* \approx 0.5H_{c2}$ in UBe_{13}, is much lower than $H_p \approx 0.9H_{c2}$, suggesting that the origin of H^* is different from that of H_p. Magnetic torque measurements by Schmiedeshoff *et al.* revealed an anomalous contribution to the magnetic torque in the field range of 3−5 T[32]. Furthermore, as mentioned in the section 2, Shimizu and co-workers observed anomalous magnetic response around $H_a \approx 0.3H_{c2}$ and pointed out that this anomaly is ascribed to either a superconducting diamagnetic anomaly or a short range ferromagnetic order in the vortex core. In any case here we stress that the surface impedance is related to the pinning effect. Details will be discussed later.

In contrast to the behavior of the low frequency, the data of 71 MHz and 97 MHz show similar behavior each other as seen in figure 6.3 and 6.4. Especially for R_s, anomalous suppression at around $H^* \approx 0.5H_{c2}$ smears out. However, the strong suppression of Rs and Xs near H_{c2} still exists.

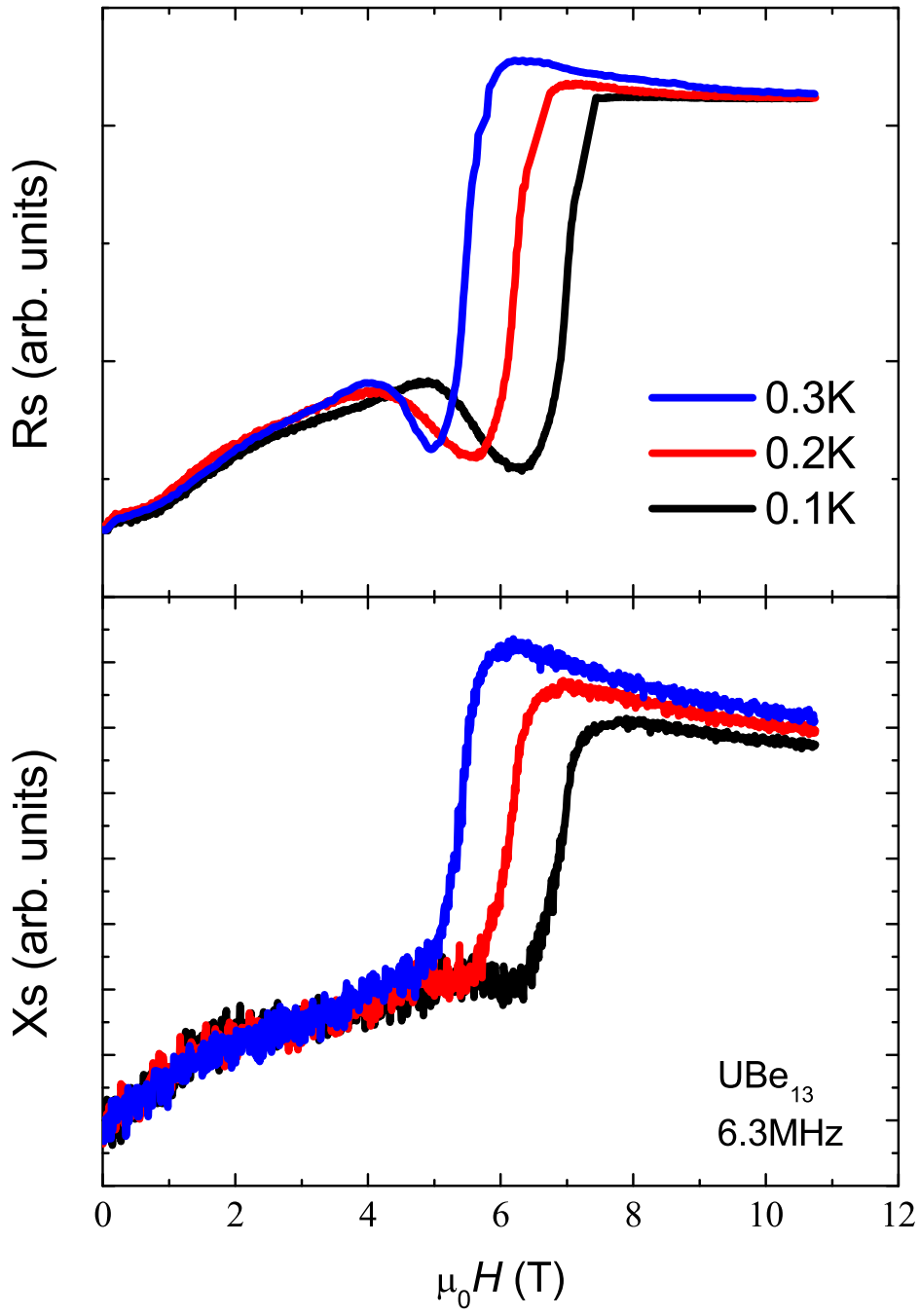


Figure6.1 The field dependence of Rs and X measured at 6.3 MHz on various temperature.

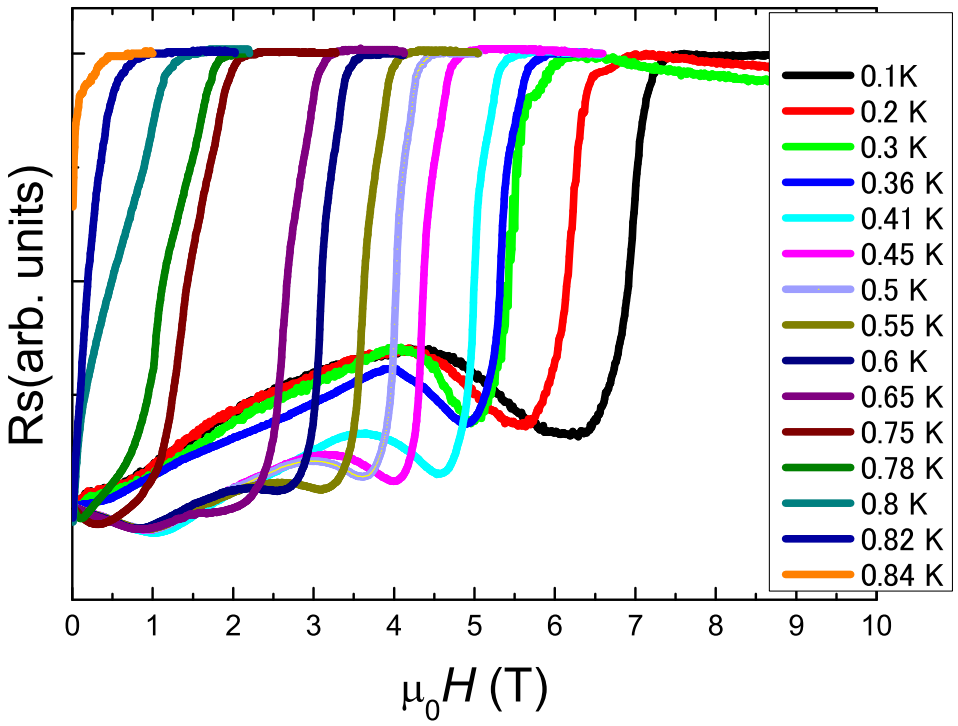


Figure6.2 The field dependence of Rs at 5.7 MHz and 6.3 on various temperature. The data of temperature range between 0.84 K and 0.36 K have been measured by Tou *et al.* and reported in [21].

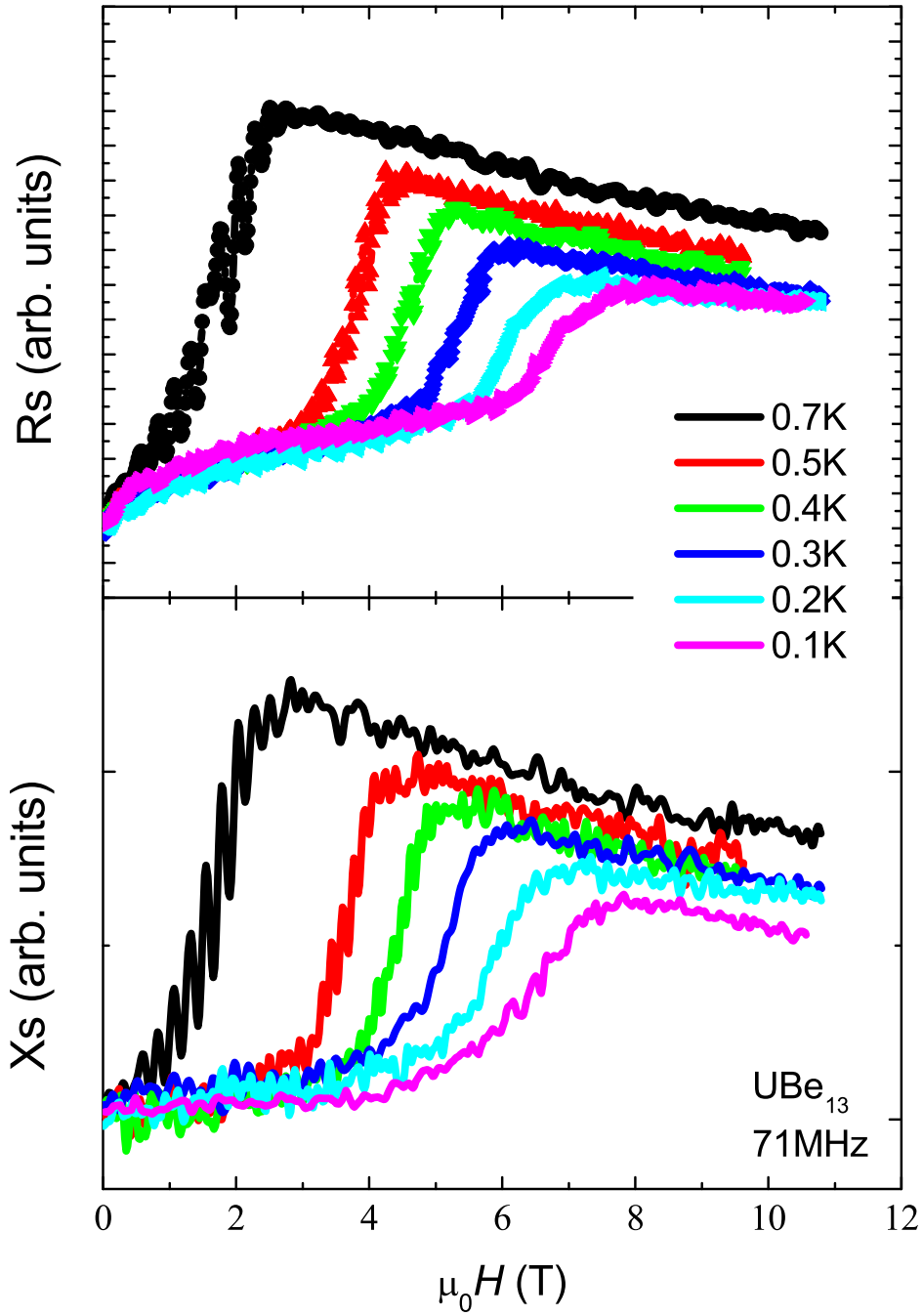


Figure6.3 The field dependence of Rs and Xs at 71 MHz on various temperature.

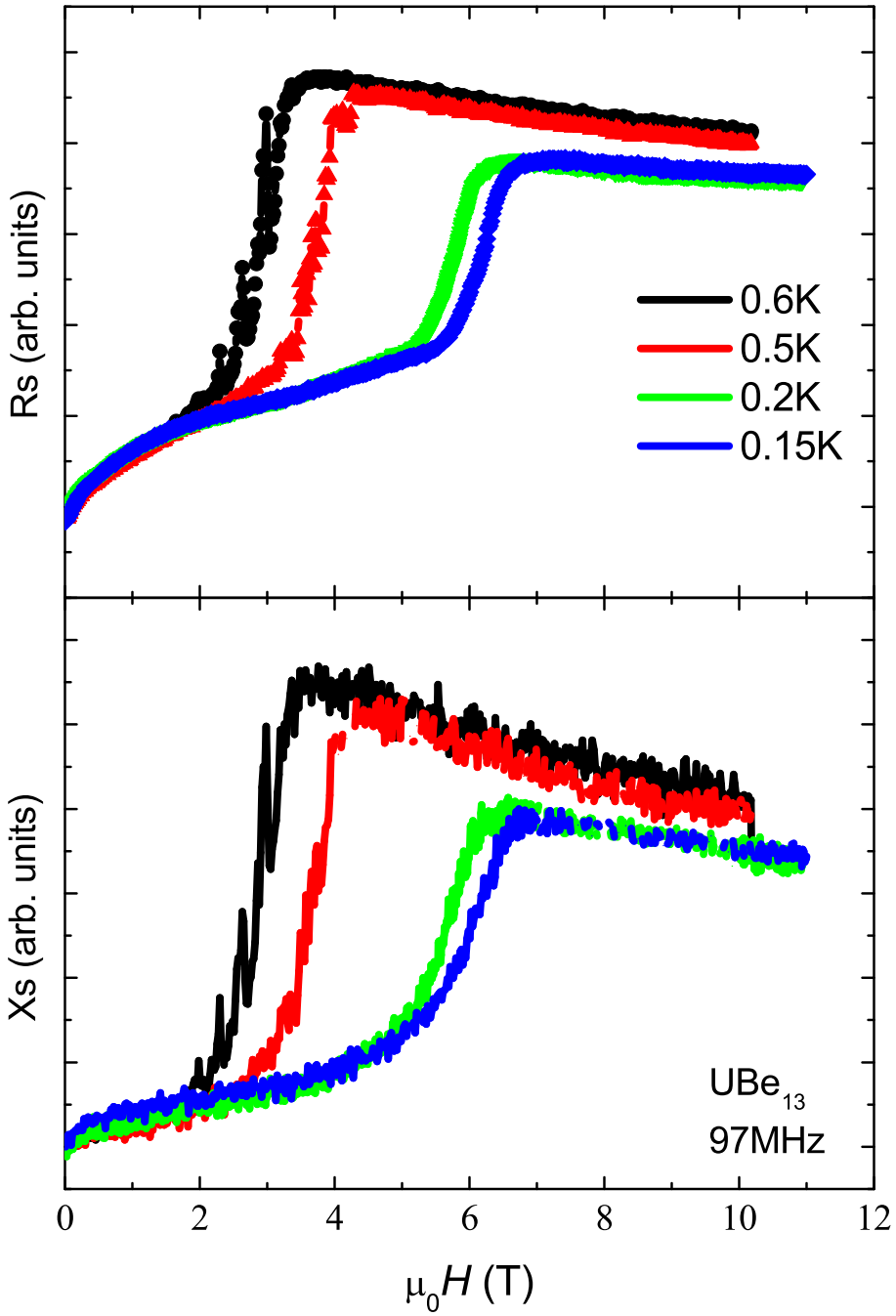


Figure6.4 The field dependence of Rs and Xs at 97 MHz on various temperature.

6.2 NMR

NMR measurements have been carried out under various fields along to [001],[110] and [111] using ^{3}He refrigerator and ^{3}He - ^{4}He dilution refrigerator.

6.2.1 H // [111]

The temperature dependence of the NMR spectra under 0.75 T, 3 T, 4 T, and 5.47 T for $H\|$ [111] have been measured and these data are shown in figures 6.5, 6.6, 6.7, and 6.8 respectively. The quadrupole interaction of Be(II) can be almost cancelled when the direction of the field is parallel to [111]. Hence, the two peaks corresponding to Be(I) and Be(II) sites can be observed. In the low field, the resonance frequency of Be(I) and Be(II) is very close and those signals overlap each other and cannot be deconvoluted. However, those two signals become distinguishable with increasing field.

The superconducting transition temperature T_c and the temperature corresponding to the anomaly, T_a, in the superconducting state are estimated from surface impedance data and are summarized in Table 2.

Table2 T_c and T_a under various field

	0.75 T	3 T	4 T	5.47 T
T_c (K)	0.81	0.65	0.55	0.36
T_a (K)	0.76	0.56	0.48	0.3

In order to compare the spectral change on passing through T_a, temperature dependences of the normalized spectra at various fields are shown in figures 6.9-6.12.

As clearly shown in the figure 6.9 measured at 0.75 T, there is no spectral change between 1 K and 0.8 K ($< T_c$). On the other hand, the linewidth of the spectra are broadened and the center of the peak position corresponding to the signals from Be(II) site shifts to low frequency side below T_a. The similar results are obtained for the data observed at 3 T and 4 T, and are shown in figure6.10 and 6.11, respectively.

As clearly shown in figure 6.12, the data measured at 5.47T, however, show no change down to the lowest temperature of 0.03 K. This result suggests that T_a for

$H\|[111]$ is less than 5.4 T.

Above 3 T, the lines corresponding to the Be(I) and Be(II) sites can be distinguishable. Differently from the NMR spectra of Be(II), the NMR spectra of Be(I) does not change at all in the observed temperature range.

From the NMR experiments for $H\|[111]$, we have found characteristic feature of the NMR spectra and the results are summarized below.

- At $H = 0.75, 3, 4$ T, Be(II)-NMR lines shift to low frequency side below T_a and the linewidth of Be(II) lines are broadened below T_a
- At 5.4 T, Be(II)-NMR lines, both peak position and line width, do not change at all on passing through T_a.
- Be(I)-NMR line site does not change at all although the Be(II)-NMR lines change below T_a.

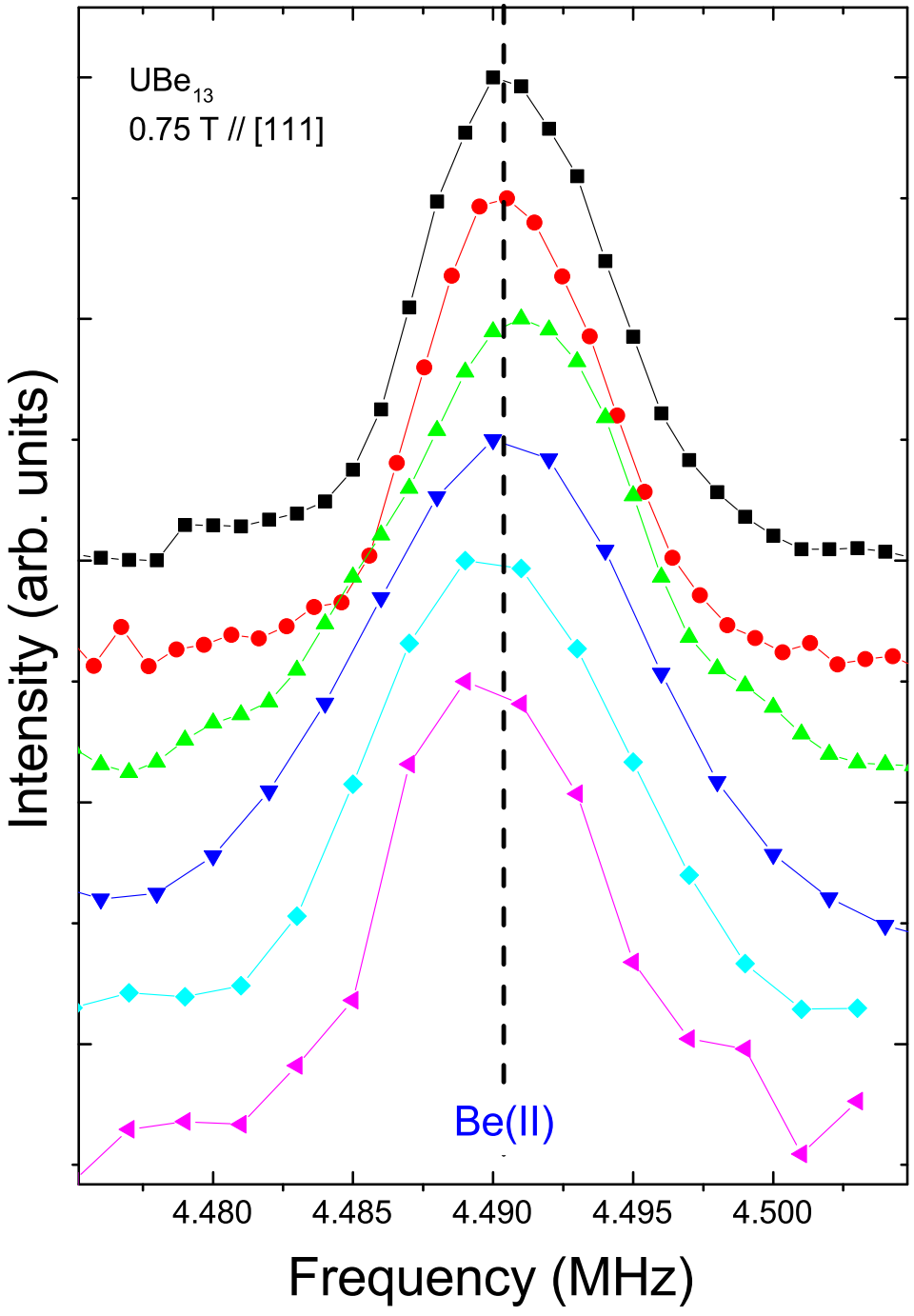


Figure6.5 The temperature dependence of spectra under 0.75 T // [111]. The dashed line is guide to eye.

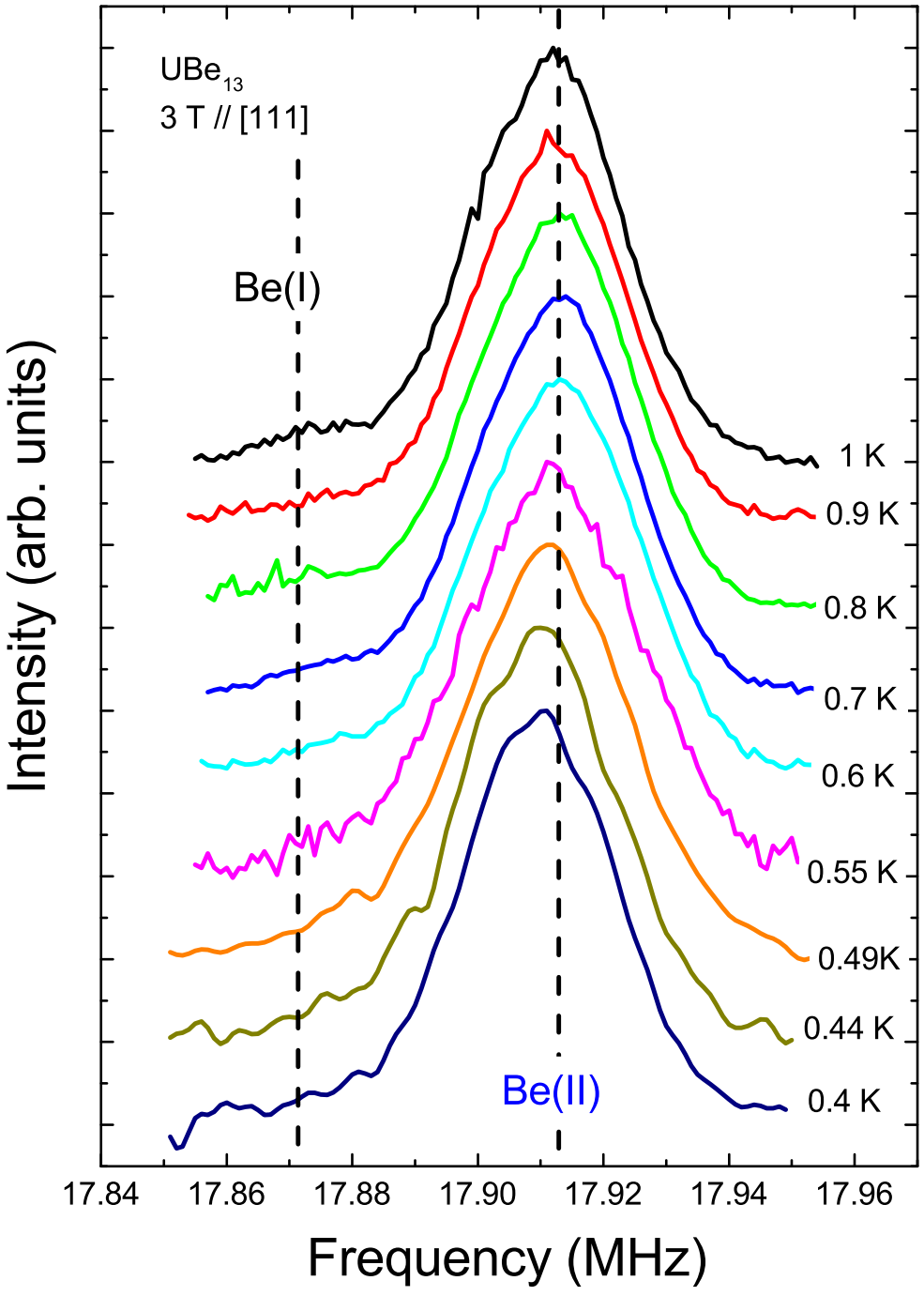


Figure6.6 The temperature dependence of spectra under 3 T // [111]. The dashed lines are guide to eye.

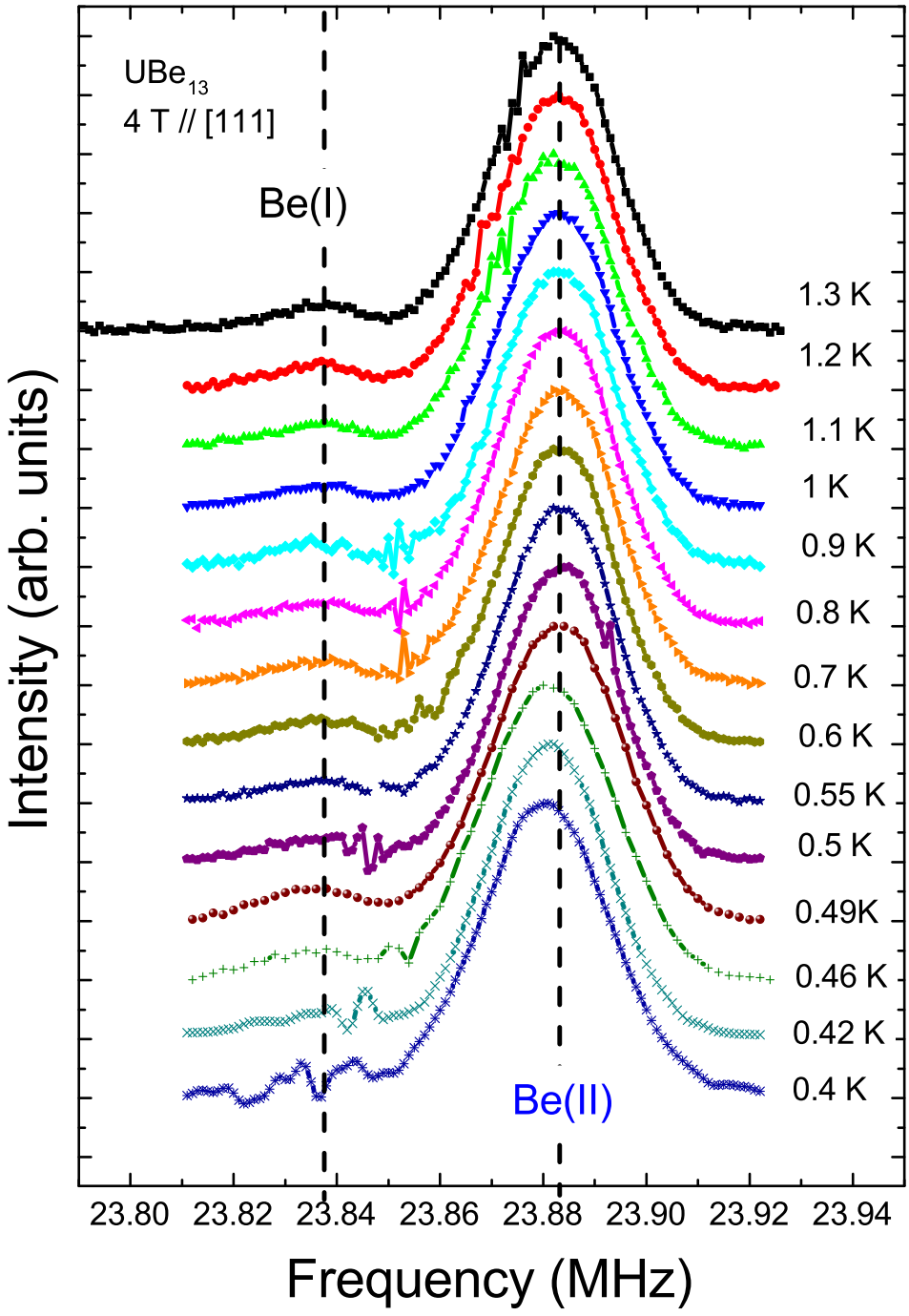


Figure6.7 The temperature dependence of spectra under 4 T // [111]. The dashed lines are guide to eye.

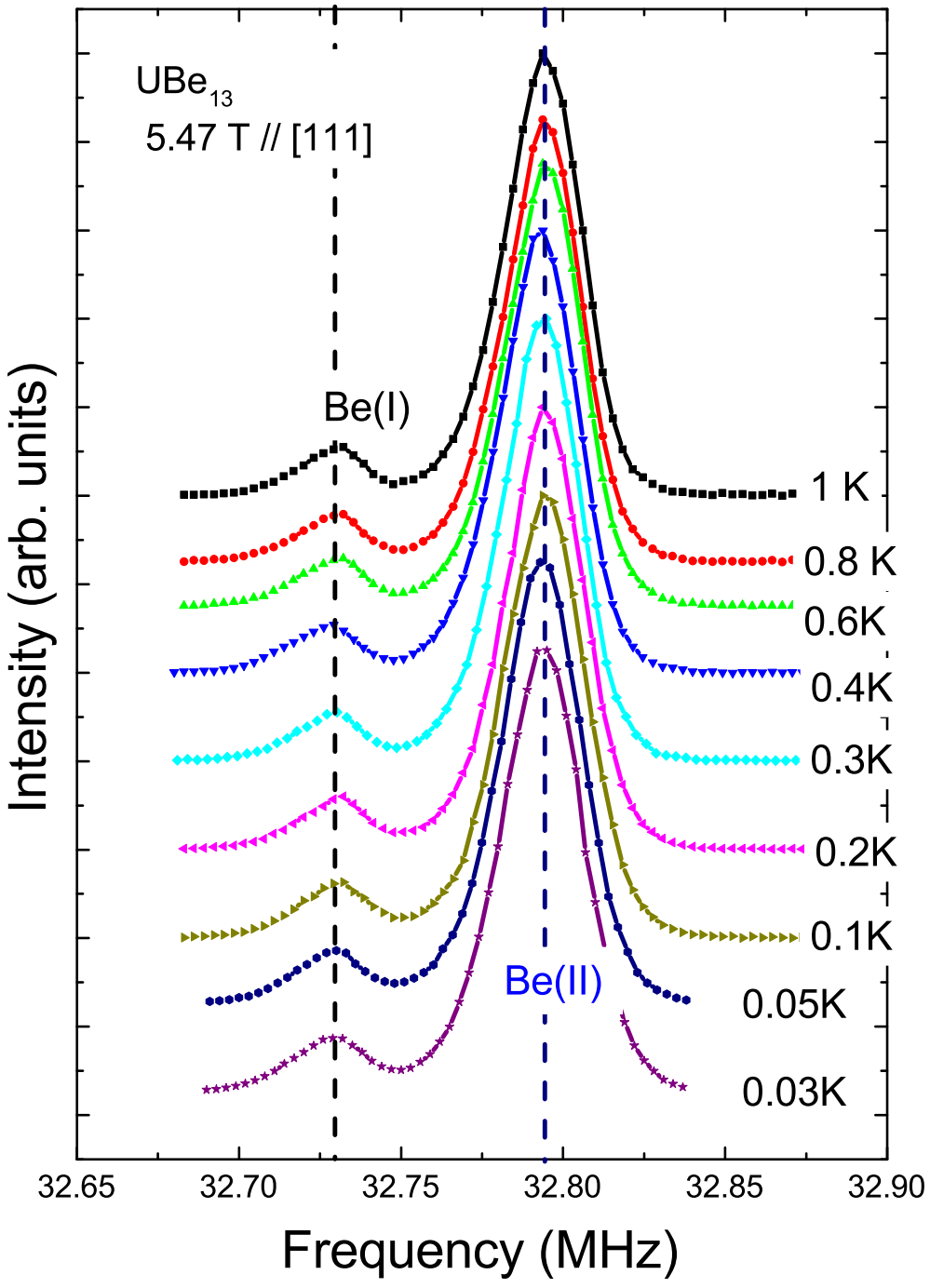


Figure6.8 The temperature dependence of spectra under 5.47T // [111]. The dashed lines are guide to eye.

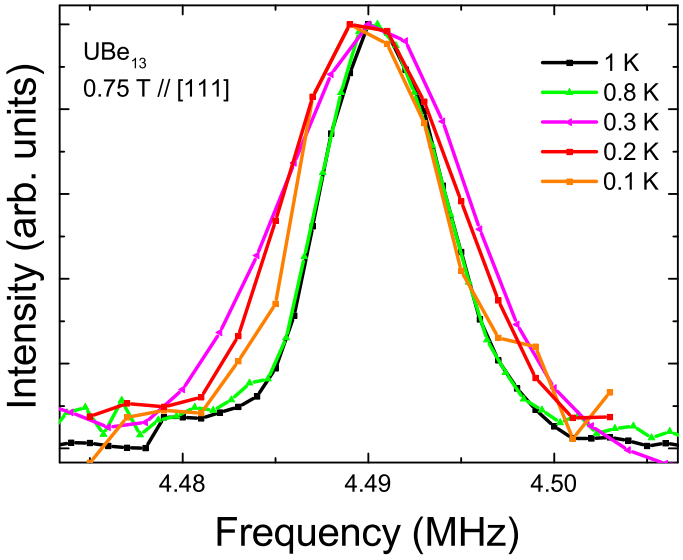


Figure6.9 The comparison of spectra at low and high temperature under 0.75 T // [111].

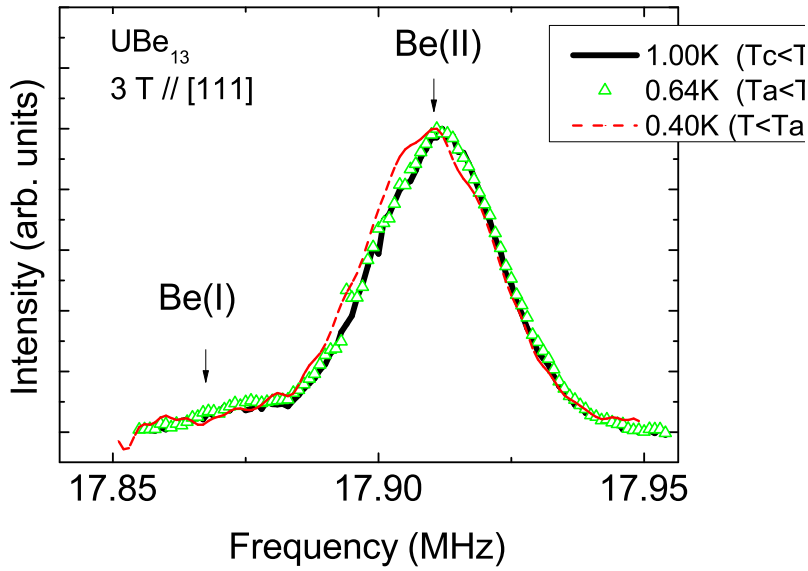


Figure6.10 The comparison of spectara at low and high temperature under 3 T // [111].

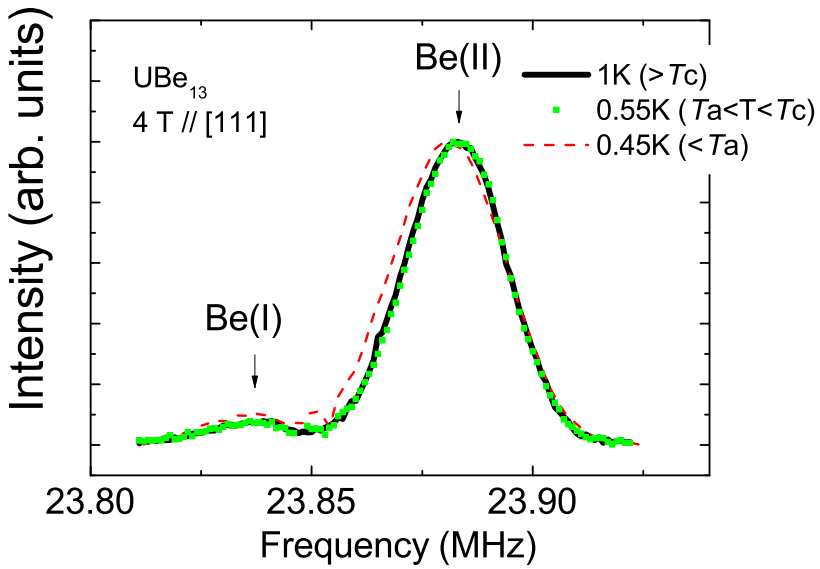


Figure6.11 The comparison of spectra at low and high temperature under 4 T // [111].

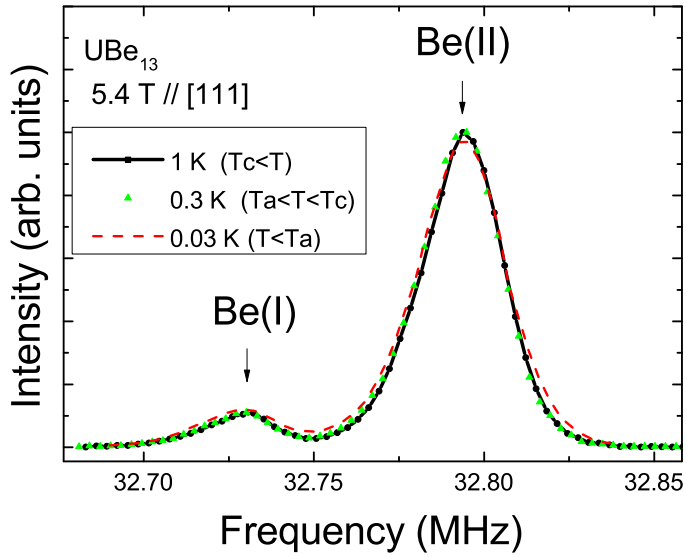


Figure6.12 The comparison of spectra at low and high temperature under 5.47 T // [111].

6.2.2 H//[110]

The temperature dependence of the NMR spectra under 0.75 T, 1.7 T, 5.2 T, and 5.47 T for $H\|$ [110] have been measured and these data are shown in figures 6.13, 6.14, and 6.15, respectively. For $\|$[110], the quadrupole interaction of Be(II) site can not be cancelled out, so that, essentially, we observe ten NMR lines. In the low field, the NMR signals from the Be(I) and Be(II) sites overlap each other and cannot be deconvoluted. However, at 5.2 T, those two signals become distinguishable because of the opposite sign of the hyperfine coupling constant.

The superconducting transition temperature T_c and the temperature corresponding to the anomaly, T_a, in the superconducting state are estimated from surface impedance data and summarized in Table 3.

Table3 T_c and T_a under various field

	1.7 T	5.2 T	5.47 T
T_c (K)	0.77	0.4	0.36
T_a (K)	0.61	0.31	0.3

Temperature and field dependences of the NMR lines are very complicated to be summarized. However here we stress that NMR line does not change at all in the temperature range between T_c and T_a. On the other hand, some peak positions, where peaks correspond to the satellites, shift to lower frequency side below T_a as shown in figures 6.16 - 6.18. Especially above 5.2 T, the Be(I) NMR lines can be deconvoluted. Although the Be(II)-NMR lines shift to lower frequency side below T_a, the Be(I) NMR lines do not shift at 0.1 K. As for $H\|$[110], the maximum T_a is estimated to be higher than 5.47 T. From the NMR experiments for $H\|$[110], we have found characteristic feature of the NMR spectra and the results are summarized below.

- In the observed field range, Be(II)-NMR lines shift to low frequency side below T_a. However the change of linewidth of Be(II) lines cannot be observed within the experimental errors.
- Be(I)-NMR line site does not change at all although the Be(II)-NMR lines

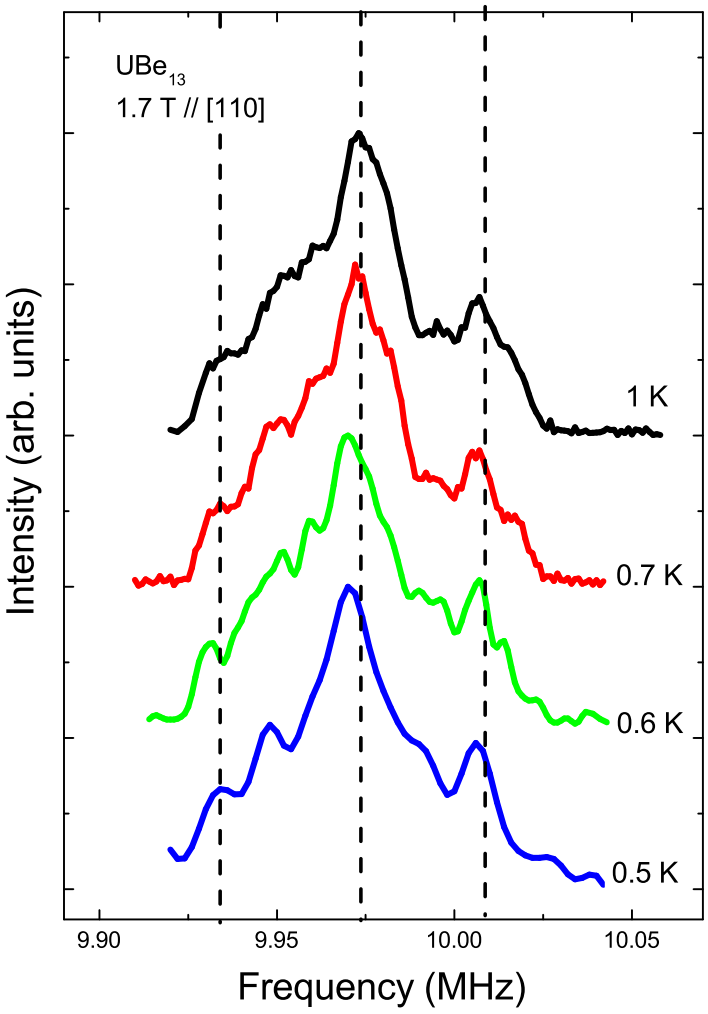


Figure6.13 The temperature dependence of spectra under 1.7 T // [110]. The dashed lines are guide to eye.

change below T_a.

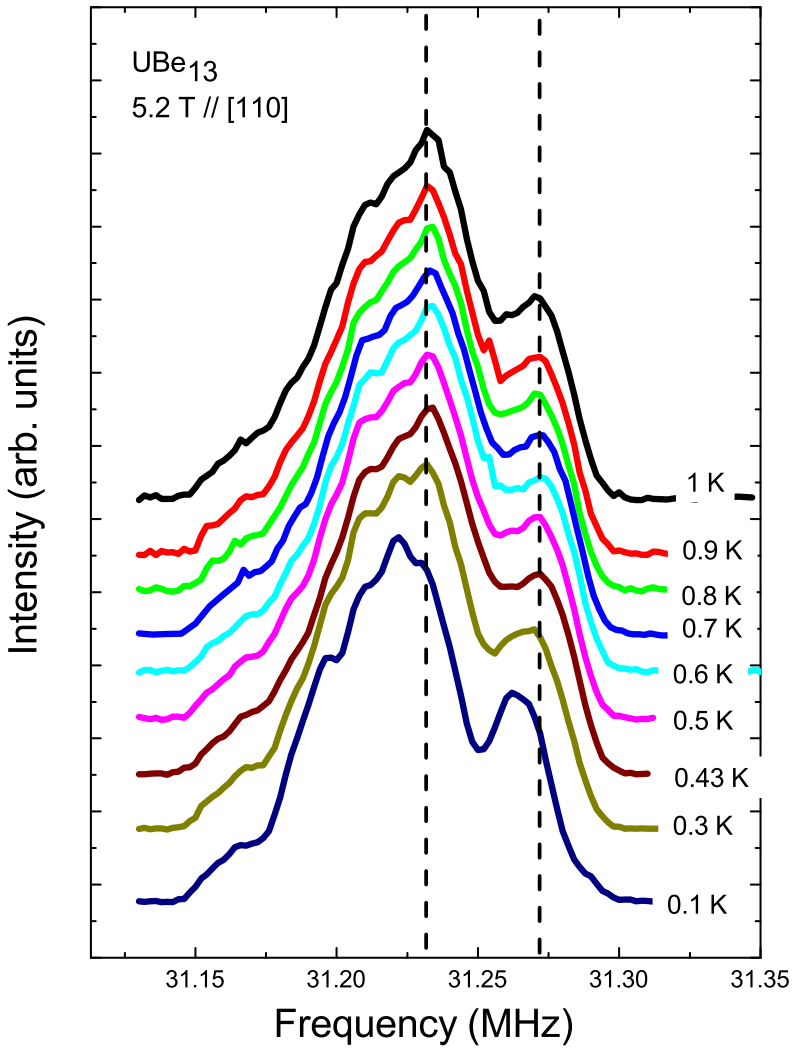


Figure6.14 The temperature dependence of spectra under 5.2 T // [110]. The dashed lines are guide to eye.

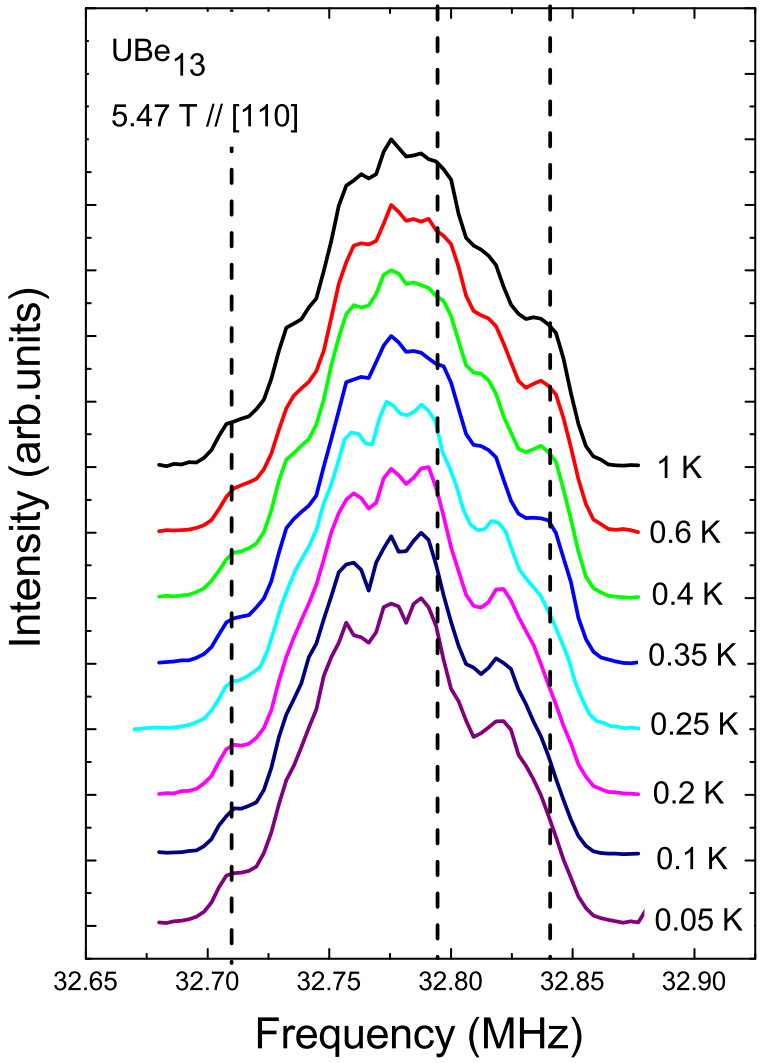


Figure6.15 The temperature dependence of spectra under 5.47T // [110]. The dashed lines are guide to eye.

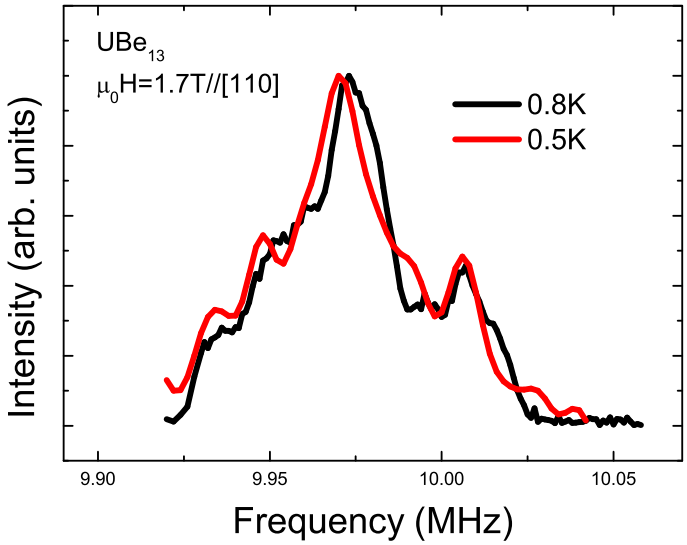


Figure6.16 The comparison of the spectra under 1.7 T // [110].

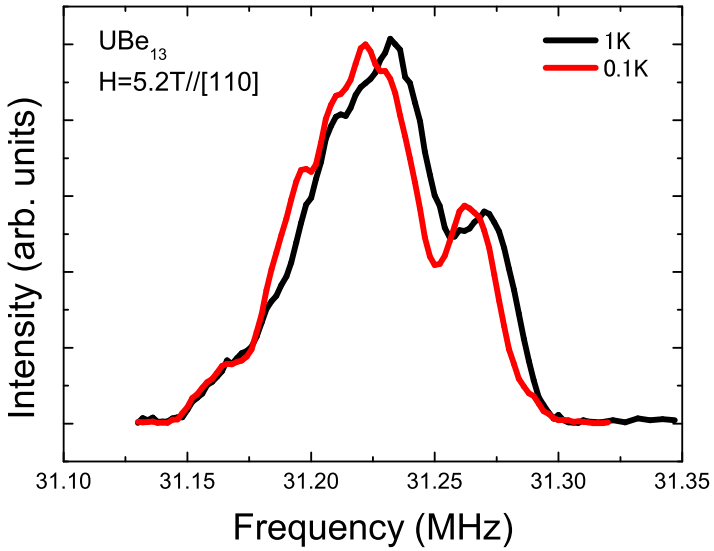


Figure6.17 The comparison of the spectra under 5.2 T // [110].

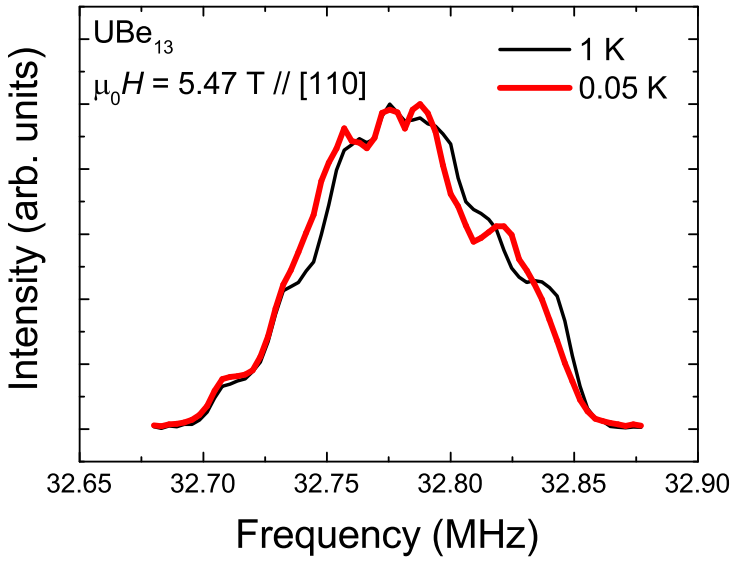


Figure6.18 The comparison of the spectra under 5.47 T // [110].

6.2.3 H//[001]

The temperature dependence of the NMR spectra under 0.9 T, 5 T, and 5.47 T for $H\|$ [001] have been measured and these data are shown in Figures 6.19, 6.20 and 6.21 respectively. For $H\|[001]$, the quadrupole interaction of Be(II) site cannot be cancelled out similarly to the case for $H\|[001]$. As for $H\|[001]$, the NMR signals from the Be(II) site are split largely by the quadrupole interaction, thus the signals from the Be(II) sites overlap with the signals from the Be(I) site.

The superconducting transition temperature T_c and the temperature corresponding to the anomaly, T_a, in the superconducting state are estimated from surface impedance data and summarized in Table 4.

Table4 T_c and T_a under various field

	0.9 T	5 T	5.47 T
T_c (K)	0.8	0.42	0.36
T_a (K)	0.75	0.36	0.3

Temperature and field dependences of the NMR lines are also complicated. Similarly to the behavior of $H\|[110]$, NMR lines do not change in the temperature range between T_c and T_a. On the other hand, the line profile changes and peak positions entirely shift to lower frequency side below T_a as shown in figures 6.22-6.24. .

From the NMR experiments for $H\|[001]$, we have found characteristic feature of the NMR spectra and the results are summarized below.

- In the observed field range, Be(II)-NMR lines shift to low frequency side below T_a with spectral broadening.
- Be(I)-NMR line site cannot be observed because of the overlap of the Be(I) and Be(II) lines.

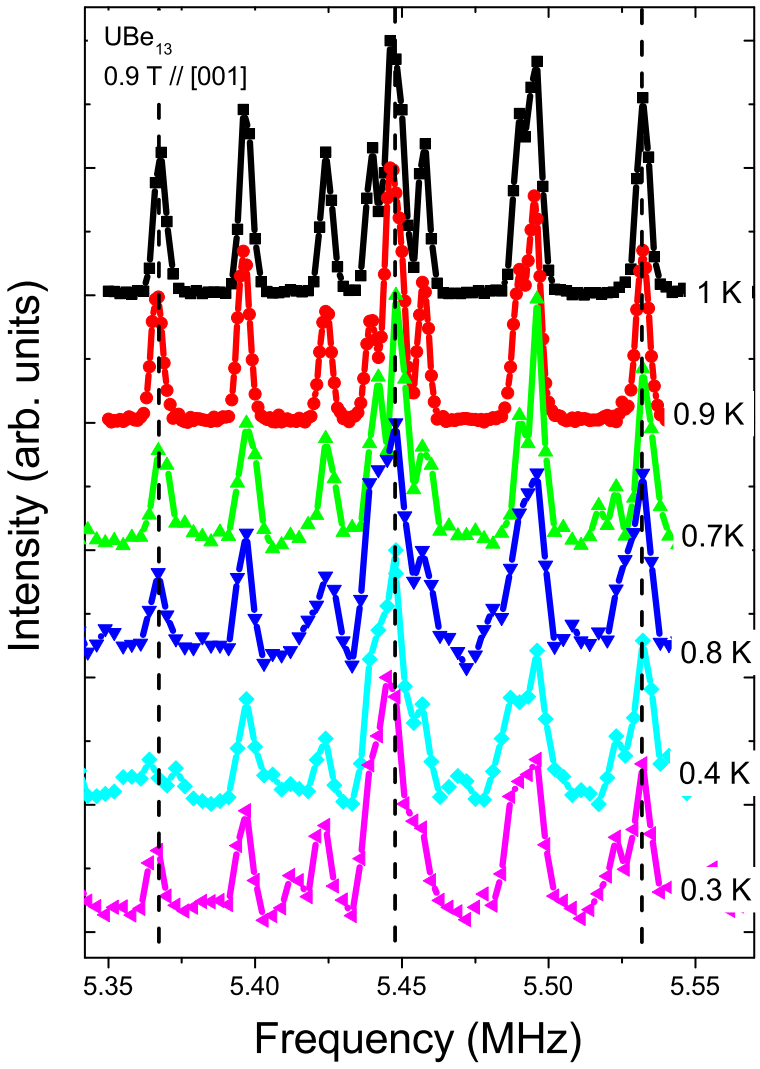


Figure6.19 The temperature dependence of spectra under 0.9 T // [001]. The dashed lines are guide to eye.

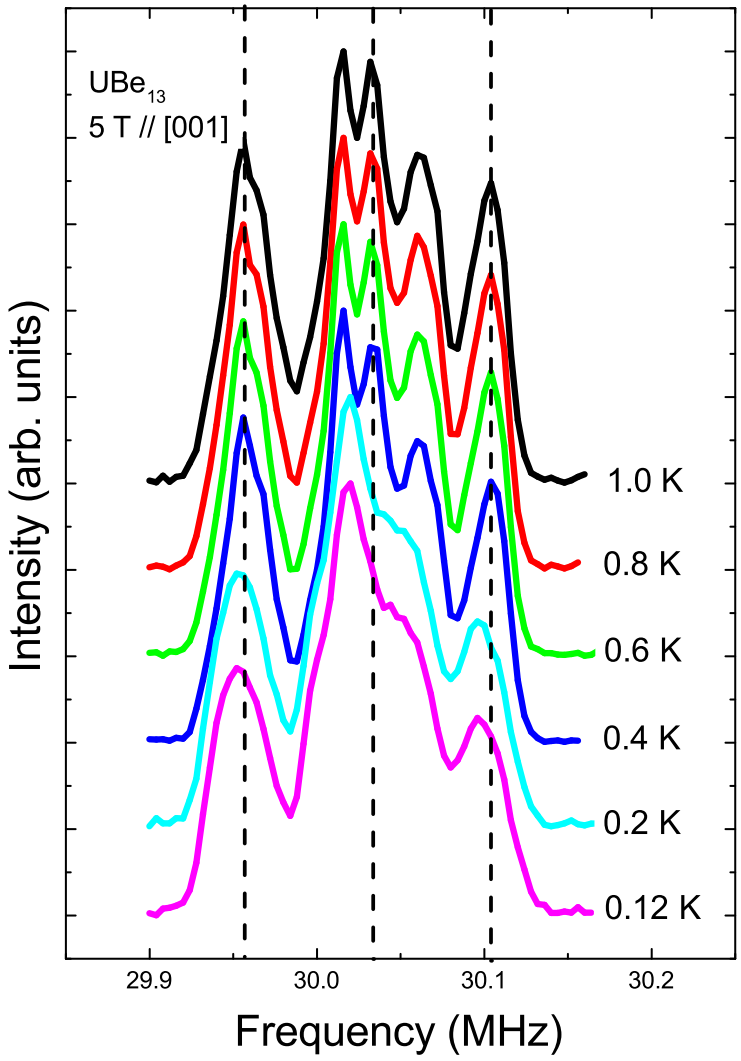


Figure6.20 The temperature dependence of spectra under 5 T // [001]. The dashed lines are guide to eye.

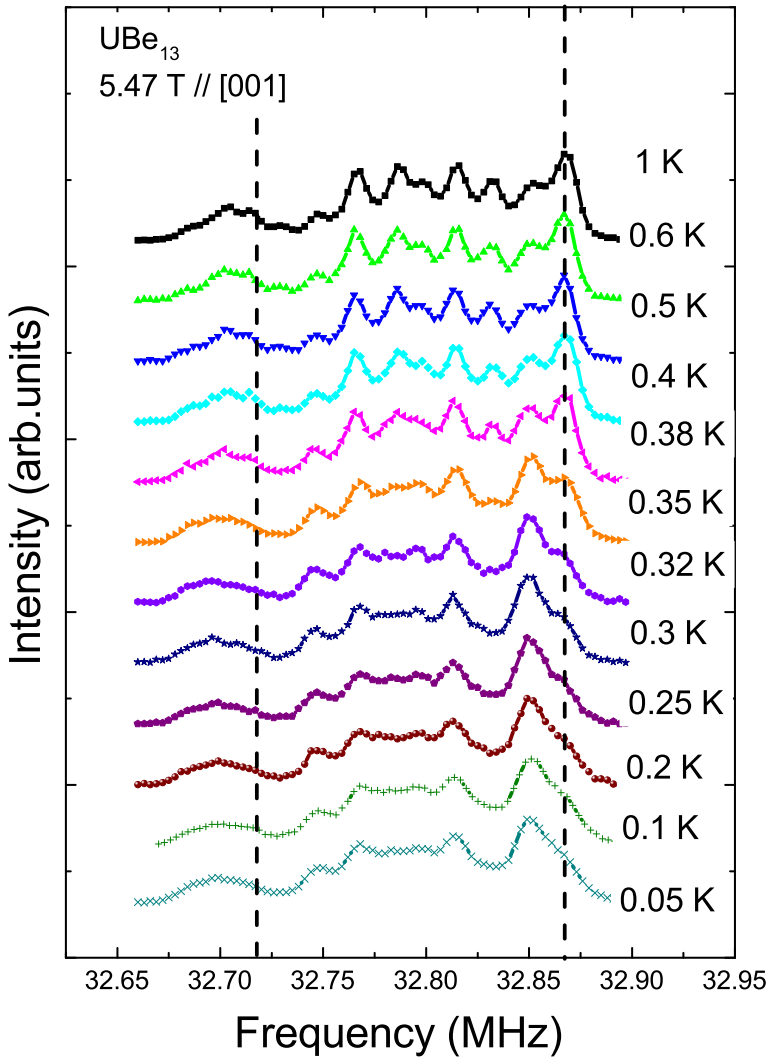


Figure6.21 The temperature dependence of spectra under 5.47T // [001]. The dashed lines are guide to eye.

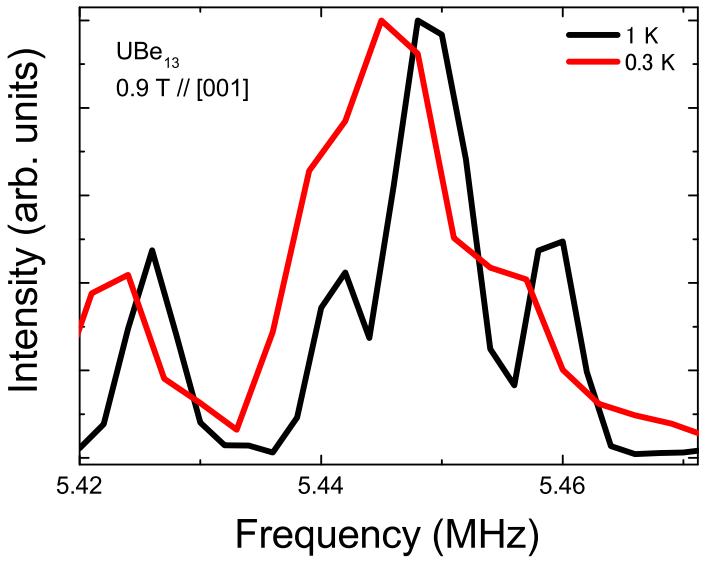


Figure6.22 The comparison of the spectra under 0.9 T // [001].

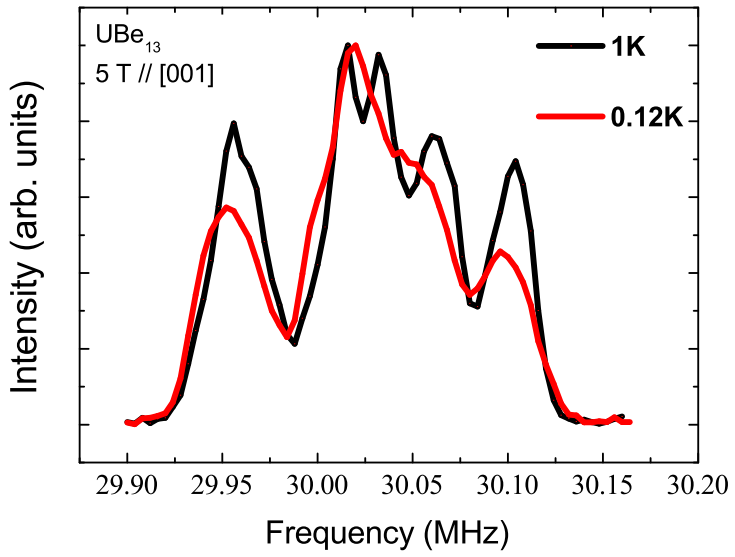


Figure6.23 The comparison of the spectra under 5 T // [001].

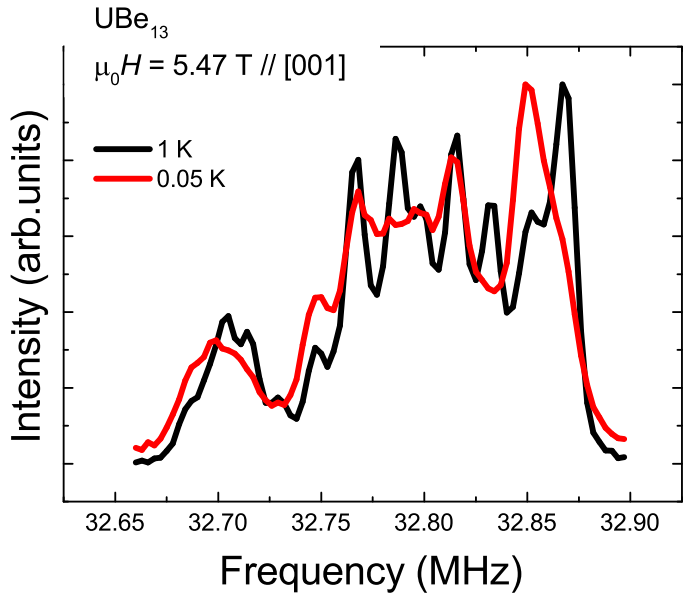


Figure6.24 The comparison of the spectra under 5.47 T // [001].

6.2.4 The nuclear relaxation rate $1/T_1$

The measurements of the nuclear spin-lattice relaxation rate $1/T_1$ under several fields have been performed and summarized in figure 6.25. The measurements of 0.75 T, 3 T and 4 T have been carried out under field for $H\|$ [111]. The measurements of 0.9 T and 5.47 T have been carried out under field in [001] and [110] respectively. The previous data of 0.8 T under field $H\|$ [111] measured by Tou *et al.* is plotted together with the present data. The solid and dotted lines indicate guide line for T^3 and T^5, respectively. The temperature dependence below T_c show the drastic decrease, which obey to $\sim T^5$. However, below 0.6 K, the temperature dependence of $1/T_1$ becomes weaker with decreasing temperature and temperature dependence is close to $T^2 \sim T^3$. The behavior of $T_1T = \text{const.}$ in low temperature region reported for the powder sample cannot be observed.

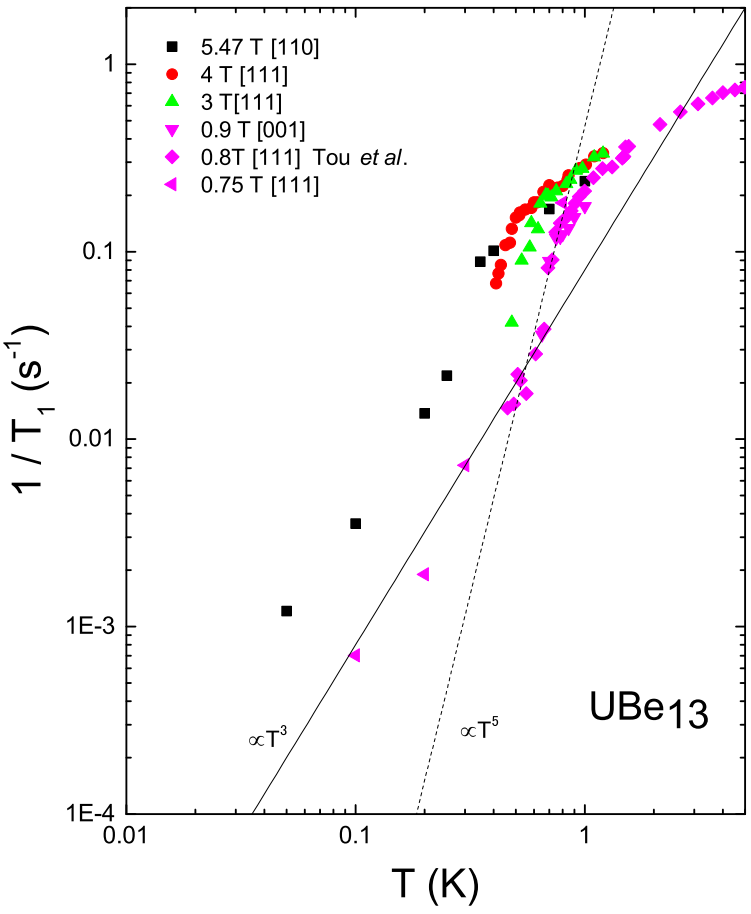


Figure6.25 The temperature dependence of $1/T_1$ under various fields.

7 Discussion

7.1 The frequency dependence of Rs

The field dependence of the R_s at 100 mK measured at several frequencies are shown in figure 7.1. The schematic of the general frequency dependence of R_s is shown in figure 7.2.

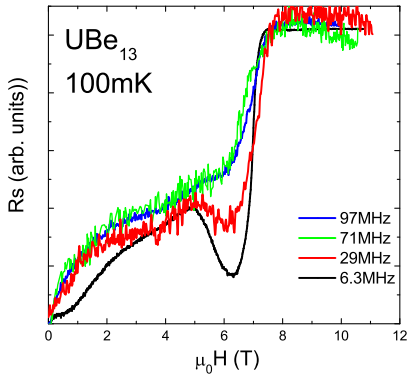


Figure7.1 The freqeuency dependence of Rs at 100 mK.

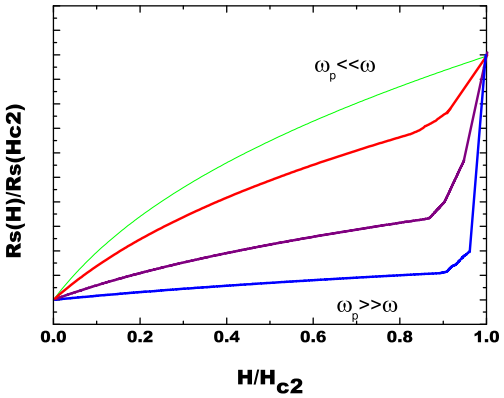


Figure7.2 The schematic of general frequency dependence of Rs.

Firstly, we focus on the frequency dependence of R_s to check the flux pinning effect. As mentioned in the section 5.2.4, for the type II superconductor in the magnetic field, a magnetic flux ϕ_0 is trapped inside in the superconducting current vortex and is quantized in a unit of ϕ_0. When electric current $\boldsymbol{j}$ is applied to the superconductor, such a vortex, which traps ϕ_0, suffers the Lorentz force of $\boldsymbol{f} = \boldsymbol{j} \times \phi_0 \boldsymbol{B}/n$, where n is the number of flux per unit volume and $B = n\phi_0$. That is, vortices per unit volume suffers the Lorentz force of $\boldsymbol{F} = n\boldsymbol{f} = \boldsymbol{j} \times \boldsymbol{B}$. Similarly, if an alternating electromagnetic field is applied to the superconductor, vortices are shaken perpendicularly to both $\boldsymbol{j}_{\mathrm{eddy}} e^{i\omega t}$ and $\boldsymbol{B}$, where $\boldsymbol{j}_{\mathrm{eddy}}$ is the eddy current due to skin depth effect. Then, vortices are driven perpendicularly to both $\boldsymbol{j}$ and $\boldsymbol{B}$ by the Lorentz force. When kind of the defects, for examples, stacking faults or impurities, etc., are absent, vortices can move freely by such Lorentz forces. Since the vortex

state is a normal state, then the motions of vortices cause the finite resistivity in the superconducting state, the so-called "free flux flow resistivity, ρ_f".

When an alternating electromagnetic field is applied perpendicularly to the external field to the metallic material, surface impedance $Z_s = X_s + iR_s$ can be obtained as stated in the section 5.2.4. In the superconducting mixed state, R_s has a finite value even in the superconducting state without defects, because of $R_s \propto \rho_f$. On the other hand, when the defects exist in the superconductor, they act as a trap against the flux motion, the so-called "pinning center". The flux motion is disturbed and the flux flow resistivity is suppressed. Such a pinning mechanism is "conventional" and the pinning force is not so strong. Then, the flux comes off the pinning center when an appropriate alternating electromagnetic field with the frequency range from MHz to GHz is applied. In such a case, R_s depends on frequency, as shown in the figure 7.2. We can know the strength of pinning force from the pinning frequency.

As clearly seen in the figure, R_s is independent of frequency above 71 MHz, indicating that the pinning effect does not occur. This result suggests that the pinning frequency is less than 71 MHz. On the other hand, with decreasing the frequency, R_s deviates from that measured at the high frequency region above 71 MHz; R_s for 29 MHz is suppressed in the field region above 2 T, although, below 2 T, R_s falls in the line with that above 71 MHz. Furthermore, R_s at 6.3 MHz is entirely suppressed in comparison with that above 71 MHz. As for the frequency-independent behavior above 29 MHz in the low field region, the "conventional" pinning frequency is estimated to be $\omega_{p1} < 30$ MHz. This value is almost consistent with $\omega_{p1} \sim 10$ MHz for heavy fermion superconductors as well as metallic superconductors having defects. We also found that there is no difference between 71 MHz and 97 MHz, but R_s for 29 MHz is more suppressed unusually in the high field region above 3 T. This suppression corresponds to the second pinning frequency of 29 MHz $< \omega_{p2} <<$ 71 MHz. Furthermore, above 3 T, R_s for both 6.3 MHz and 29 MHz show two minimal points at around 3.8 T and 6.1 T. R_s for 71 MHz and 97 MHz also have weak minimal points even though the free flux flow state is realized above 71 MHz. These behaviors are quite different from those for the "conventional pinning" as shown in the figure 7.2. Therefore the unusual frequency and field dependences of R_s is attributed to the other mechanisms than the "conventional" pinning effect.

The unusual behaviors of R_s are summarized as follows.

(a) The unusual suppressions of $R_s(H)$ at H_{a1} and H_{a2} occur against the strength of the applied field but rather than the frequency. This feature is suggestive of the pinning of the flux motion is induced by the magnetic field. The field H_{a2} is almost consistent with the field at which bulk physical properties show anomaly. On the other hand, NMR data exhibit anomalies at around H_{a1}.

(b) Above 71 MHz, $R_s(H)$ does not depend on frequency, suggesting the free-flux flow state within the frame work of the conventional theory. This feature indicates that the anomalies are not attributed to the "conventional" pinning effect but rather to the change of the ρ_f (Rs $\propto \rho_f$) itself.

Above two characteristic features strongly suggest that the suppressions of R_s at H_{a1} and H_{a2} are ascribed to the change of the value of the ρ_f.

In general, ρ_f relates to the coherence length ξ, mean free path l, Fermi energy E_F and superconducting gap Δ. When the superconducting gap(Δ) satisfies the relation of

$$\xi \ll l < \xi E_F \Delta(0),$$

ρ_f can be expressed by following formula, [33, 34].

$$\rho_f(H) = \frac{\mu H}{\langle \omega(k) \rangle \tau n |e| c} \frac{k_B T_c}{\Delta(T)},$$

where τ, and n are the relaxation time of quasiparticle and the carrier density of quasiparticles in the core of vortex. $\langle \omega(k) \rangle$ reflects the gap structure around the vortex.

To discuss the flux flow resistivity, the mean free path l of UBe_{13} is important. Simply, the large residual resistivity suggests $l \approx 20$ Å within the frame work of the free electron model. In this case, the above theory should be modified and it cannot be utilized as it is, because the all excitations should include into the flux flow resistivity. However, this estimation is oversimplified. Brison and coworkers evaluated that the pair breaking parameter from the thermal conductivity and they estimated $l \approx 10^5$ Å[35]. This value is surprisingly large but their claim was that the simple estimation for l breaks down in UBe_{13} and l is much larger than the coherence length. Furthermore, by using the normal state resistivity of $\rho \approx 200 \mu\Omega$cm[11] and band structure calculation[36], more reliable l can be estimated as several hundreds

angstroms. This is because the carrier density of UBe_{13} is small as 0.25 carrier per unit cell[11, 36]. In this context, above theoretical formula holds for the present case.

To explain the unusual behavior of R_s, the parameters of either $\langle\omega(k)\rangle$, τ, or n should become large (small) with decreasing (increasing) magnetic field from those in the normal state (those in the superconducting state).

(i) Change of $\langle\omega(k)\rangle$

If the symmetry of the superconducting gap changes at H_{a1} with increasing magnetic field, $\langle\omega(k)\rangle$ can change. However, this contradicts with the present NMR results both for Be(I) and Be(II) sites as discussed in the later section.

(ii) Change τ

If some inelastic scatterings becomes significant at H_{a1} with increasing field, the relaxation time τ should becomes shorter. In fact, previous NMR relaxation measurements indicated that magnetic fluctuations develop with increasing magnetic field[2, 37]. Hence the change of the τ is one of possible reason for the suppression of R_s without the contradiction. For example, the superconductivity coexist with some magnetically ordered state, e.g., magnetically ordered vortex core, [20] etc., below H_{a1}, the magnetic fluctuations are suppressed below H_{a1}. When the magnetically ordered state is destroyed by the magnetic field above H_{a1}, magnetic fluctuations appear and contribute inelastic scattering. Then, τ becomes shorter above H_a

(iii) Change of n

If some (short range) ferromagnetic ordered state in side in the vortex core transitions to the paramagnetic state at H_{a1} with increasing field, the carrier density in the normal core suddenly decreases at H_{a1} with increasing field. However, this contradicts with the results of NMR Knight shift at Be(I) site as will be discussed in the later section.

(iv) both τ and n

UBe_{13} is believed to be a multi-band superconductor. In this case, bands from small Fermi surface can be easily affected with magnetic field. If a superconductivity with a small gap for a band corresponding to a small Fermi surface is destroyed at H_{a1} by applying magnetic field, then normal carriers should increase. Thus, multi-band effect cannot explain $\rho(H)$.

From above discussions, the present surface impedance study strongly suggests that the correlation time τ changes associated with some magnetic transition.

7.2 NMR

7.2.1 Normal state

We performed the spectral simulation calculation to assign observed spectra in normal state under field ∥ [001] and [110]. The resonance frequencies for each Be sites were calculated by exact diagonalization of the 4 × 4 nuclear spin Hamiltonian matrix of ^{9}Be as follow,

$$\mathcal{H} = \mathcal{H}_z + \mathcal{H}_Q - \gamma_n \hbar I \cdot \tilde{K} \cdot H_0 - \gamma_n \hbar I \cdot H_d \tag{36}$$

The first term represents to the Zeeman interaction expressed as equation (7) as mentioned in the section 5.1. The second term corresponds to the nuclear quadrupole interaction expressed as equations (9) and (13). The third term is due to the hyperfine interaction described by the second rank Knight shift tensor $\tilde{K}$ expressed as equations (10) and (11). Here, $\tilde{K}$ is composed of the isotropic part K_{iso} and the anisotropic part $K_i (i = 1, 2, 3)$. The last term is the classical dipolar interaction between nuclear spin and the dipole field arising from the localized U spin moment μ.

Table5 The using parameter in spectral simulation. Here, $K^{\mathrm{I}}_{\mathrm{iso}}$, $K^{\mathrm{II}}_{\mathrm{iso}}$ are isotropic part of Knight shift of Be(I) and Be(II) respectively.

ν_Q (MHz)	μ (μ_B/U)	$K^{\mathrm{I}}_{\mathrm{iso}}$	$K^{\mathrm{II}}_{\mathrm{iso}}$	K_1	K_2	K_3
0.82	0.026	-0.1	0.12	-0.07	0.01	0.06

Obtained NMR and NQR parameters are summarized in table 5. Within the experimental accuracy, we found that the parameters are independent of magnetic field and simulations using above parameter set can reproduce the obtained NMR spectra well.

In the low field region, as shown in the figure 7.3 calculated NMR line is in good agreement with the observed spectrum. At high fields, the magnitude of the NMR intensity cannot be reproduced by the simulation but the resonance frequency can be almost reproduced by simulation in all experimental results.

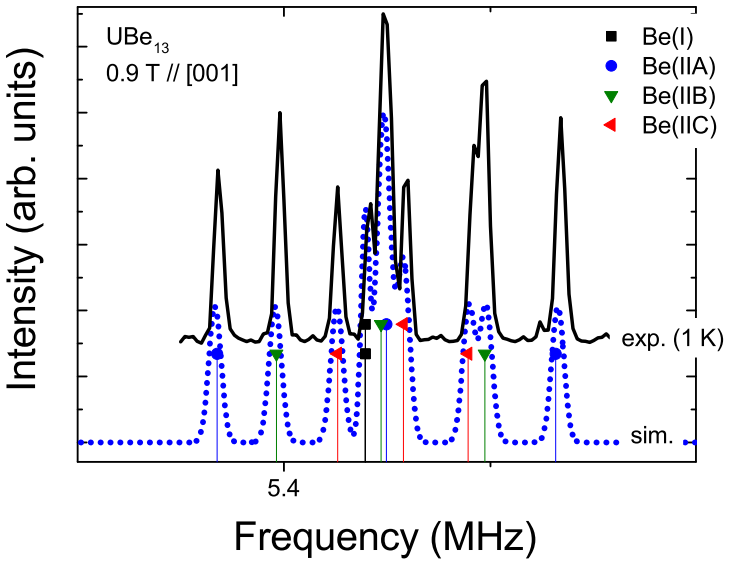


Figure7.3 The simulation of spectra of 0.9 T // [001].

7.2.2 superconducting state

The NMR lines of the Be(II) site clearly shift below T_a except the line measured at 5.47 T.

From the spectrum simulations, we also estimate the Knight shift at 3 T and 4 T for $H\|[111]$, and the results are shown in Figs.7.9, 7.10 together with the results of $1/T_1$. The superconducting states under various magnetic fields are represented by gray region. Furthermore, we found that the Knight shifts (or spectra) exhibit anomalies at T_a, below which the area is colored by blue. $1/T_1$ clearly decreases below T_c, which coincides with the temperature estimated from the bulk measurements. On the other hand, the Knight shift shows the constant behavior. The reduction of $1/T_1$ below T_c is direct evidence that the bulk superconductivity occurs below T_c. With further decreasing temperature, the Knight shift decreases at T_a.

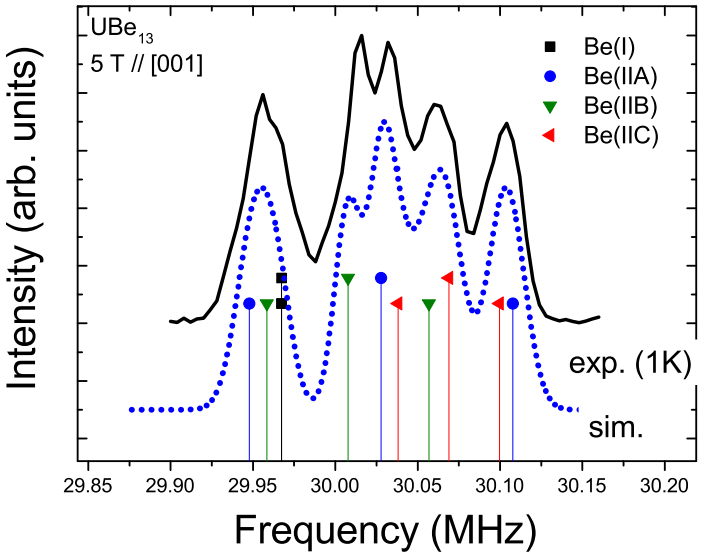


Figure7.4 The simulation of spectra of 5 T // [001].

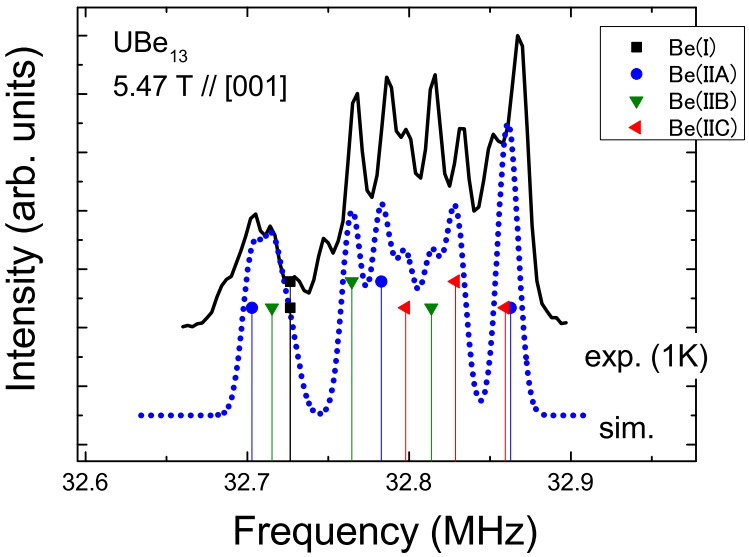


Figure7.5 The simulation of spectra of 5.47 T // [001].

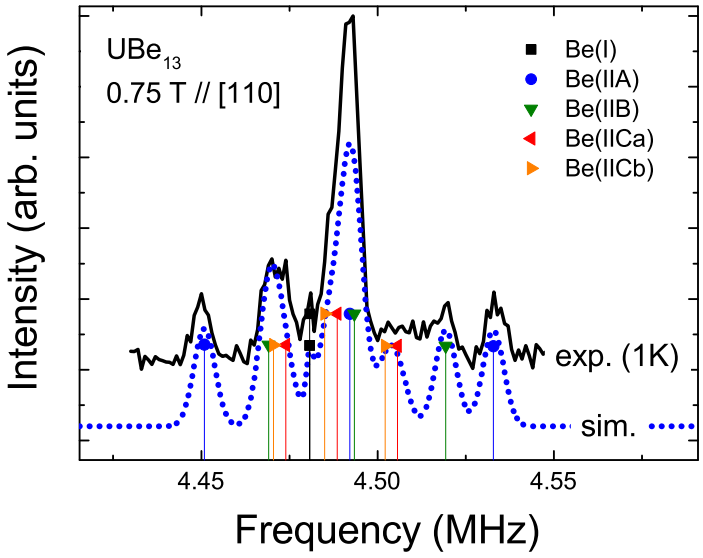


Figure7.6 The simulation of spectra of 0.75 T // [110].

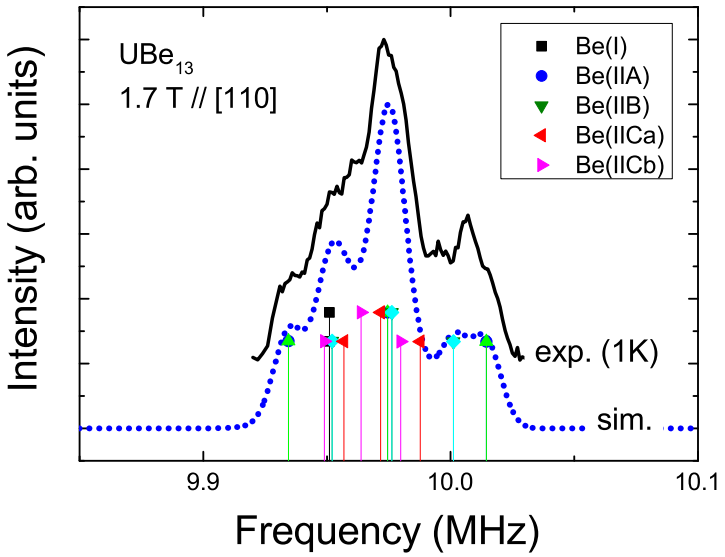


Figure7.7 The simulation of spectra of 1.7 T // [110].

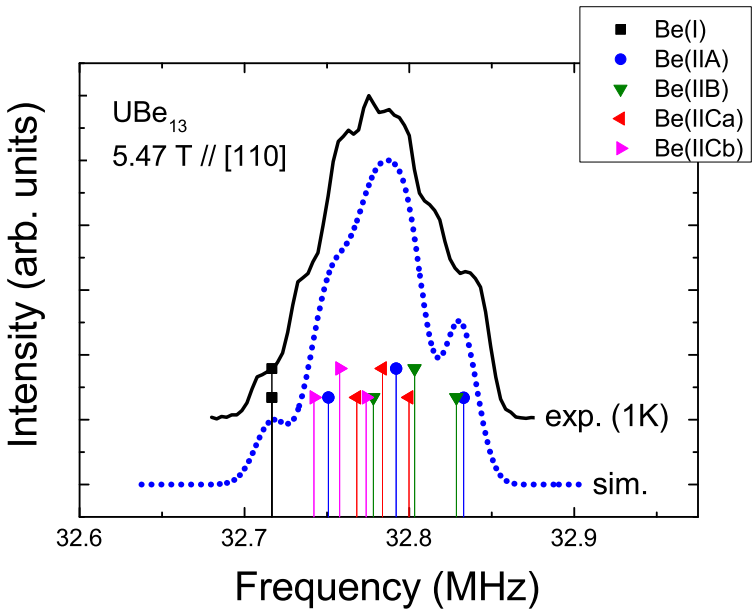


Figure7.8 The simulation of spectra of 5.47 T // [110].

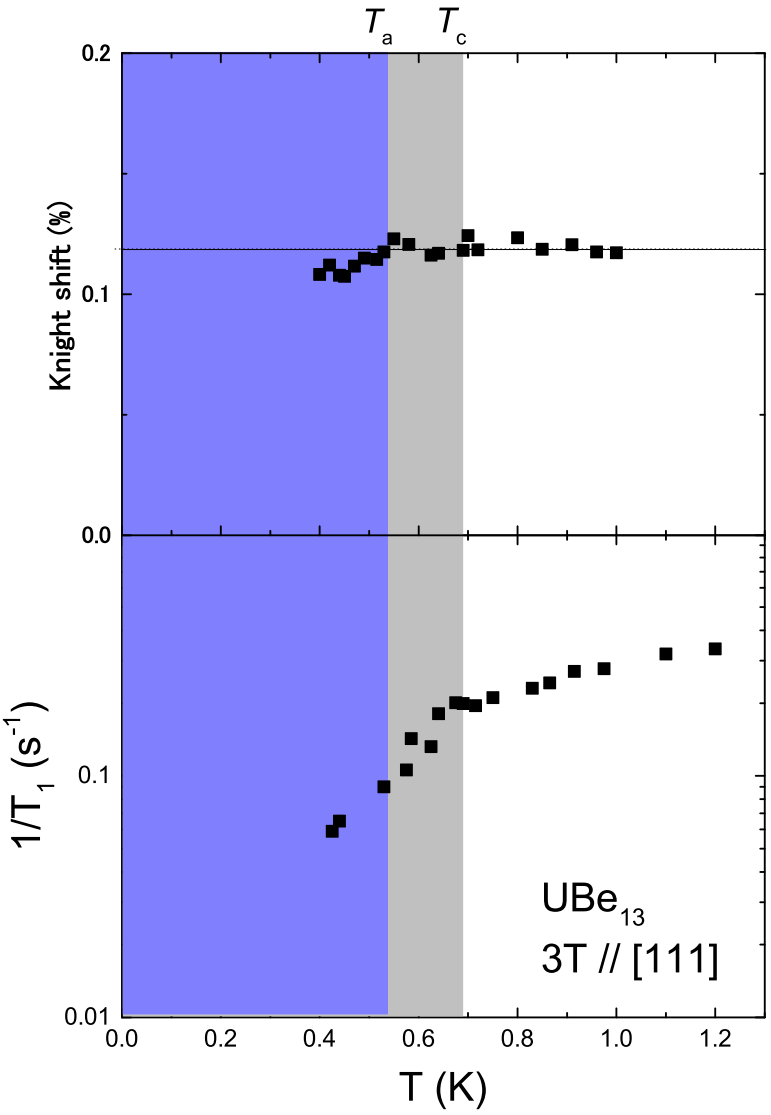


Figure7.9 The temperature dependence of Knight shift under 3 T // [111].

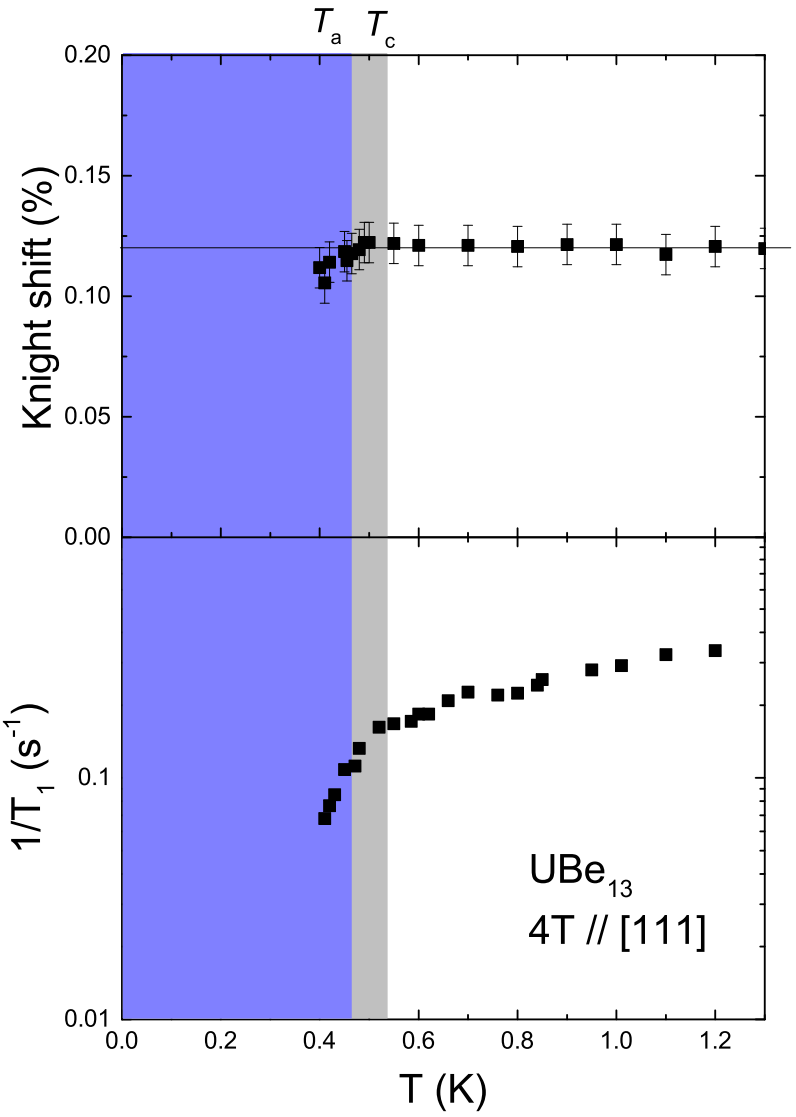


Figure7.10 The temperature dependence of Knight shift under 4 T // [111].

In general, the decrease of the Knight shift in the superconducting state is explained by the formation of the spin-singlet pairing state. In the present case, the simple spin-singlet scenario is excluded because the Knight shift does not change below T_c whereas $1/T_1$ decrease markedly.

As possible explanations for the unusual decrease of the Knight shift below T_a are follows.

scenario (1)

An even-parity order parameters develop below T_a, similarly to the case of UPt_3 having degenerated odd-parity order parameters.[22]

scenario (2)

A freezing of the triplet d-vector to the crystal axes.

scenario (3)

A certain ordering occurs below T_a

As for the anomalies in temperature dependence of the Knight shift at T_a, several possible mechanisms can be considered. The one of the possibilities, which can explain the anomaly in SC state, is the effect of the vortex state.

Since UBe_{13} is the type II superconductor, the observed field range, which exceeds $H_{c1} \sim 50$ Oe, is the superconducting mixed state. Then the triangular vortex lattice state is expected in the mixed state, and the local field distributes interior in the sample. Especially for the low field region, such a field distribution is prominent as follows.

$$H_{loc}(\boldsymbol{r}) = H_0 \sum_G \frac{\exp\left(-i\boldsymbol{G}\cdot\boldsymbol{r} - \boldsymbol{G}^2\xi^2\right)}{1+\boldsymbol{G}^2\lambda^2}, \tag{37}$$

Where $\boldsymbol{G}$, ξ and λ are reciprocal lattice vector, coherence length and field penetration depth, respectively. This filed distribution causes the spectra broadening, the so-called "Redfield pattern".

The calculations for the Redfield pattern spectra at 0.75 T and 3 T for $\parallel$ [111] are shown in figure 7.11 and 7.12, respectively, together with the experimental data. Here, we used $\lambda = 4400$ Åand $\xi = 60$ Å.

At 0.75 T, the calculated mixed-state line broadens slightly in comparison with the experimental data. However, at 0.1 K, the observed NMR line broadens more than the calculated line. Moreover, the simulation at 3 T does not show any broadening.

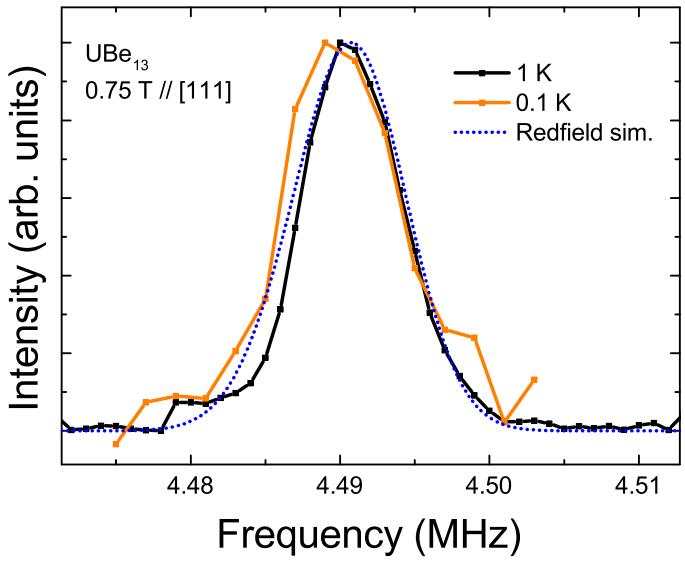


Figure7.11 The simulation of Redfield pattern of 0.75 T.

This is a consequence of the large λ and small ξ. Thus the scenario (1) is excluded.

Furthermore, we stress here that the Be(I) line around 17.75 MHz and at 0.4 K in the superconducting state is consistent with the line at 1 K. If the anomalous decrease in the Be(II) Knight shift at T_a relates to the change of the superconducting state, the spectra of the Be(I) site should change below T_a as same as that of the Be(II) site. However, the peak position and line width of the Be(I) site under fields of 3 T and 4 T show no change below T_a. The scenario (2) is excluded because the Knight shift for Be(I) site should decrease below T_a. In this case, the hyperfine coupling constant is negative and its magnitude is the almost the same as that at the Be(II) site.[5]. Namely, the Knight shift for the Be(I) site increase below T_a, and the 1/10 line width should decrease below T_a. However, such a spectral change cannot be detected. Therefore, these results are direct evidence that the origin of the Knight shift anomaly at T_a is not ascribable to the superconductivity but to some magnetic or electric order. That is, the scenario (3) is most plausible.

Again, the Knight shift related to the superconductivity does no change at all on passing through both T_c and T_a. This result provides unambiguous evidence that the spin triplet superconducting state is realized in UBe_{13}. In particular, the Knight shift

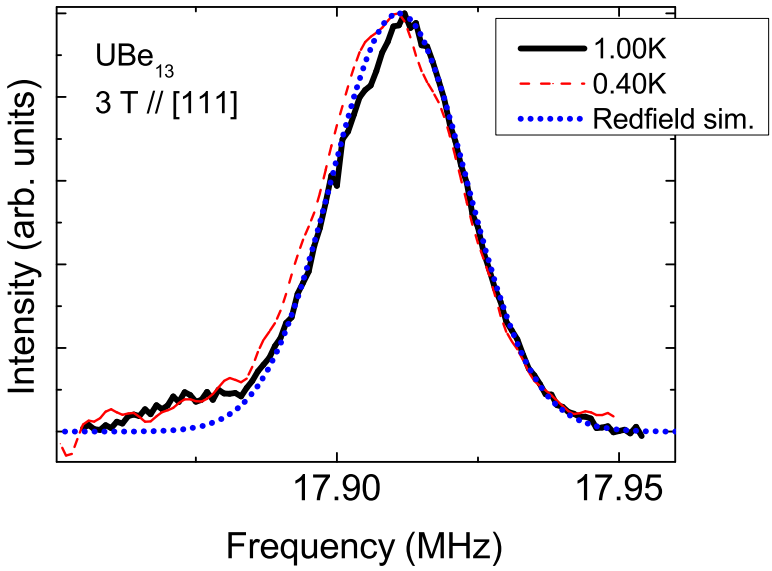


Figure7.12 The simulation of Redfield pattern of 3 T.

at 5.47 T for $H\|$ [111], which shows no change down to 0.03 K far below T_c, supports this idea.

Rather, it is reasonable to consider that the spectral broadening at low temperatures is attributed to an extra effect, i.e. scenario (2).

As mentioned above, the change of the NMR spectra can be observed only for the Be(II) site, while the spectra for the Be(I) site does not change. If the Be(II) Knight shift anomalies are originated in some ordering, it should be an antiferromagnetic like order to explain the difference between the Knight shift for the Be(I) site and that for the Be(II) site. These ideas are consistent with the result of neutron scattering measurements that propose the antiferromagnetic fluctuations exist[38].

It is necessary to understand the ground state of UBe_{13} to consider what kind of ordering occurs. Unfortunately, CEF state of UBe_{13} is not clear because of the itinerant nature of $5f$-electron state. In fact, the neutron scattering measurements fail to observe the CEF level. Theoretically, either Γ_3 CEF doublet or Γ_1 CEF singlet ground state have been proposed[39, 40, 41]. The former CEF ground state has multipoles degree of freedom, such as quadrupole and octupoles[39]. This model can explain weak magnetic response as well as non-Fermi Liquid behavior. Furthermore,

a magnetic octupole ordering may occur at low temperatures.

On the other hand, as for the latter case, Γ_1 singlet ground state is expected from the recent investigations for the Th-dope UBe_{13}[42]. The Γ_1 singlet ground state is magnetically intact and leads no magnetic and electric orderings. However, when the Γ_5 CEF first-excited magnetic triplet state, which stays closely to the ground state level, is taken into account, the quasi-degenerated quartet sate has multipoles degree of freedom, such as quadrupoles, octupoles and hexadecapoles. In fact, $PrOs_4Sb_{12}$ has the quasi-quartet ground state consisting of the Γ_1 singlet ground state and $\Gamma_4^{(2)}$ triplet excited state, and it shows the field induced antiferroquadrupole ordered state[43]. If such a quasi quartet state is realized in UBe_{13}, higher order magnetic order, such as a octupole order, can occur.

Considering with the results of neutron scattering experiments, which observed an antiferromagnetic fluctuations, an octupole ordering is a possible candidate account for the anomalous behavior of the Knight shift in UBe_{13}. However, the clearly phase transition cannot be observed by specific heat. This contradiction still remains to be clarified at the present stage.

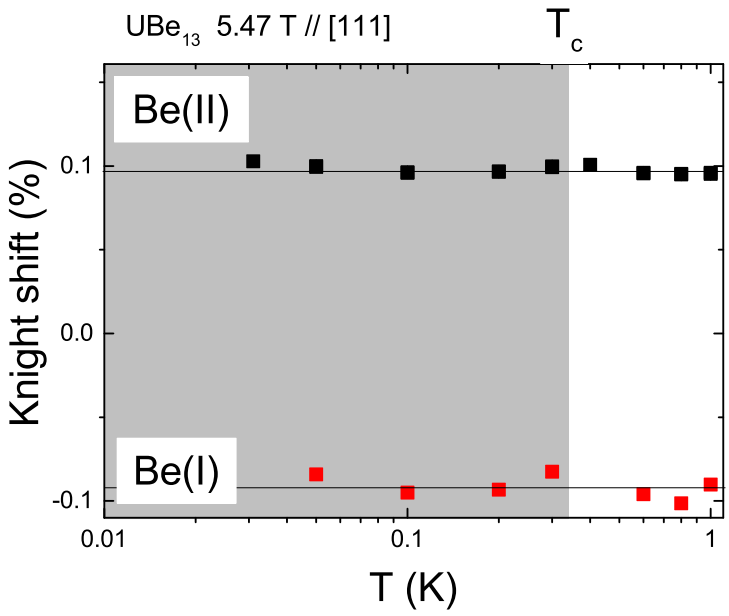


Figure7.13 The temperature dependence of Knight shift under 5.47 T // [111].

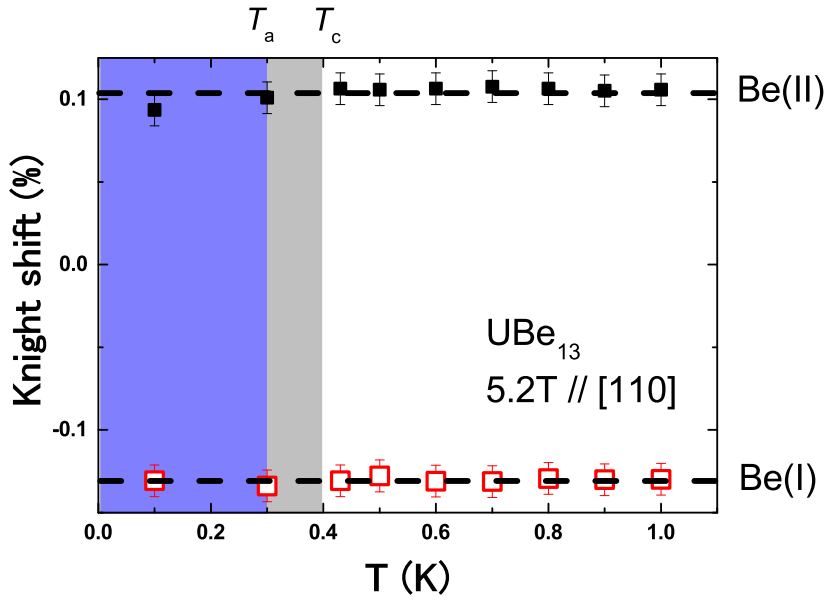


Figure7.14 The temperature dependence of Knight shift under 5.2 T // [110].

7.3 Superconductivity symmetry

In this part, we discuss about the symmetry of the superconducting order parameter. In the UBe_{13}, the Knight shift anomaly appears at T_a in the superconducting state and this anomaly disturbs determining of the symmetry of superconductivity. In the present study, we also measured the NMR spectra and T_1 under various fields and field directions.

As mention above, the Knight shift results indicate a spin triplet Cooper pairing state in UBe_{13}. On the other hand, previous μSR measurement reported that the Knight shift decreases below T_c[44], which is contradict with our results.

However, our Knight shift data provide that the reduction of the Knight shift is due to the weak internal field possibly by a higher magnetic multipole order. In this case, μSR Knight shift also change below T_a. This is a possible explanation for the contradiction between the NMR Knight shift and μSR Knight shift. In any case, μSR experiments at high fields above 5 T is needed to confirm this possibility.

Figure 7.15 shows the scaling plot of T/T_c vs. $1/T_1/1/T1(H_{c2})$. The temperature

dependence of $1/T_1$ is in proportion to $T^2 \sim T^3$ at low $T(\ll T_c)$. This result suggests that UBe_{13} has either the nodal gap with line node at Fermi surface or multi-band $s_{\pm}$ gap as reported by Iron Pnictides[45, 46]. If the UBe_{13} has a nodal gap, the density of state is induced by field as Doppler effect under field. In this case, $1/T_1$ should be enhanced and the behavior of $1/T_1T = const$ should be observed with increasing field. However, the present data show no field dependence. This behavior is reminiscent of that for the iron pnictides and suggests that the superconducting gap is expected to be a multi-band full-gap state. This is consistent with a multi-band full-gap superconductivity suggested from specific heat measurement[10]. However, our data are insufficient to conclude that whether or not multi-band full-gap is realized.

In theoretical studies, the superconducting gaps which have point nodes along the [111] directions are suggested from the band structure calculations[47, 48]. In this case, the quasiparticle excitations in UBe_{13} show full-gap-like behavior. This is because the group theoretical works predict that several odd-parity gap functions only have point nodes along [111][49, 50, 51, 52]. Especially, typical example is superfluid ^{3}He, in which the superfluid state has a full-gap and a spin triplet state, the so-called "BW" state. However, in this case, the Knight shift should decrease below T_c until $\sim 2/3\chi_p$. Here, χ_p is magnetic susceptibility of quasi particle. The results of UBe_{13} is different from case of ^{3}He. The superconducting state in UBe_{13} is unusual associated with the multi $5f$-orbitals having multipole degrees of freedom, as well as the nature of multiband inUBe_{13}. In any case, to determine the gap structure of UBe_{13}, further detailed studies are needed.

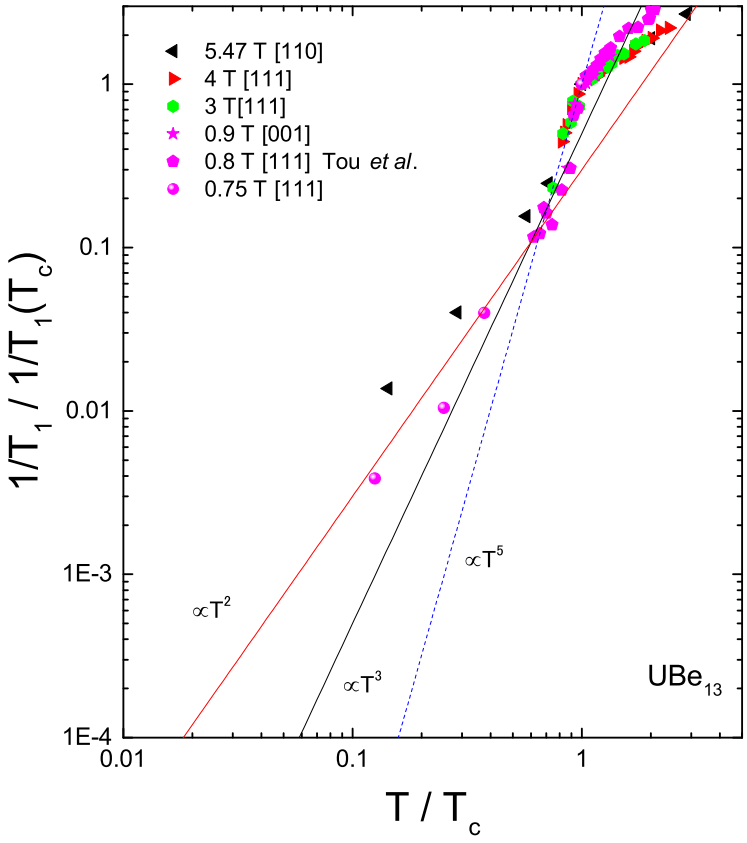


Figure7.15 The temperature dependence of normalized $1/T_1$.

8 Conclusion

The RF surface impedance and ^{9}Be-NMR measurements have been carried out on the heavy fermion superconductor UBe_{13}.

The magnetic field and frequency dependences of the surface resistance R_s have been measured. $R_s(H)$ is independent of the frequency above 71 MHz, indicating the free flux flow state is realized at least above 71 MHz. However, the field dependence is unusual differently from the conventional superconductors. The drastic change of R_s can be observed below H_{c2}. We discuss the flux flow resistivity in the case of the moderate clean limit that is suggested from the resistivity and thermal conductivity measurements. Together with the NMR results, the origin of the anomalous flux flow resistivity is attributed to the change of the quasiparticle lifetime τ. τ is expected to become shorter above H_{a1} because the magnetic fluctuation in the paramagnetic state due to the transition from a magnetically ordered state.

We have also carried out ^{9}Be-NMR under the various strength and direction of magnetic field. The present NMR measurements clarified that the Knight shift for the Be(II) sites decreases for all directions below T_a. On the other hand, the Knight shift for the Be(I) site does not change at all. These result suggests that

scenario (1)

An even-parity order parameters develop below T_a, similarly to the case of UPt_3 having degenerated odd-parity order parameters[22].

scenario (2)

A freezing of the triplet d-vector to the crystal axes.

scenario (3)

A certain ordering occurs below H_{a1}.

The scenarios (1) and (2) are excluded, while the scenario (3) is realized in the superconducting state. A discussion taking account of possible CEF states, the anomaly observed in the Knight shift is attributed to a higher order magnetic multipole state, e.g. an octupole order. On the other hand, the Knight shift does not change at all for any field strength and directions between T_c and T_a, indicating that the superconducting pairing symmetry is a spin triplet state.

We also measured temperature dependences of the nuclear spin lattice relaxation rate $1/T_1$ under several fields. $1/T_1$ shows the drastic decrease below T_c and these results indicate the bulk superconducting state regardless of the unchanged of the Knight shift in the temperature range between T_c and T_a. The Knight shift anomalies at T_a does not originate in superconductivity but also some antiferromagnetic like ordering when the results of the neutron scattering experiments is taking into consideration. Discussions of the multipoles degree of freedom assuming a CEF ground state suggest that the ordering is an octupole order. However the proof of the phase transition cannot be observed from the specific heat measurement. To confirm what kind of ordering occurs below T_a, further detailed measurements are needed.

References

[1] H. R. Ott, H. Rudigier, Z. Fisk and J. L. Smith, Phys. Rev. Lett. **50**, 1595 (1983).

[2] Kyohei Morita. Master's thesis, Graduate School of Science, Kobe University, (2012).

[3] J. Bardeen, L.N. Cooper and J.R. Schrieffer, Phys. Rev. **108**, 1175 (1957).

[4] P.W. Anderson and P. Morel, Phys. Rev. **123**, 1911 (1961).

[5] H. Tou, N. Tsugawa, M. Sera, H. Harima, Y. Haga and Y. Ōnuki, J. Phys. Soc. Jpn. **76**, 024705 (2007).

[6] Y. Haga, E. Yamamoto, T. Honma, A. Nakamura, M. Hedo, S. Araki, H. Ohkuni and Y. Ōnuki, Physica B **259-261**, 627–628 (1999).

[7] H. R. Ott, H. Rudigier, T. M. Rice, K. Ueda, Z. Fisk and J. L. Smith, Phys. Rev. Lett. **52**, 1915 (1984).

[8] D. E. MacLaughlin, C. Tien, W. G. Clark, M. D. Lan, Z. Fisk, J. L. Smith and H. R. Ott, Phys. Rev. Lett. **53**, 1833 (1984).

[9] D. Einzel, P.J. Hirschfeld, F. Gross, B. S. Chandrasekhar, K. Andres, H. R. Ott, J. Beuers, Z. Fisk and J. L. Smith, Phys. Rev. Lett. **56**, 2513 (1986).

[10] Y. Shimizu, S. Kittaka, T. Sakakibara, Y. Haga, E. Yamamoto, H. Amitsuka, Y. Tsutsumi and K. Machida, Phys. Rev. Lett. **114**, 147002 (2015).

[11] J.P. Brison, J. Flouquet and G. Duetscher, J. Low Temp. Phys. **76**, 453 (1989).

[12] Y. Shimizu, Y. Haga, T. Yanagisawa and H. Amitsuka, Phys. Rev. B **93**, 024502 (2016).

[13] M. B. Maple, J. W. Chen, S. E. Lambert, Z. Fisk, J. L. Smith, H. R. Ott, J. S. Brooks and M. J. Naughton, Phys. Rev. Lett. **54**, 477 (1985).

[14] U. Rauchschwalbe, U. Ahlheim, F. Steglich, D. Rainer and J. J. M. Franse, Z. Phys. B **60**, 379 (1985).

[15] I. A. Fomin and J. P. Brison, J. Low. Phys. Temp. **627**, 119 (2000).

[16] J. P. Brison, A. Ravex, J. Flouquet, Z. Fisk and J. L. Smith, J. Mag. Mag. Mat. **76-77**, 525 (1988).

[17] F. Kromer, R. Helfrich, M. Lang, F. Steglich, C. Langhammer, A. Bach, T. Michels, J. S. Kim and G. R. Stewart, Phys. Rev. Lett. **81**, 4476 (1998).

[18] C. Wälti, E. Felder, H. R. Ott, Z. Fisk and J. L. Smith, Phys. Rev. B **63**, 100505(R) (2001).

[19] B. Ellman, T. F. Rosenbaum, J. S. Kim and G. R. Stewart, Phys. Rev. B **44**, 12074(R) (1991).

[20] Y. Shimizu, Y. Haga, Y. Ikeda, T. Yanagisawa and H. Amitsuka, Phys. Rev. Lett. **109**, 217001 (2012).

[21] H. Tou, N. Tsugaw, M. Doi, Y. Nakai and M. Sera, J. Phys. Soc. Jpn. **75**, Suppl. 201–203 (2006).

[22] Y. Machida, A. Itoh, Y. So, K. Izawa, Y. Haga, E. Yamamoto, N. Kimura, Y. Ōnuki, Y. Tsutsumi and K. Machida, Phys. Rev. Lett. **108**, 157002 (2012).

[23] M. Lang, R. Helfrich, F. Kromer, C. Langhammer, F. Steglich, G.R. Stewart and

J.S. Kimi, Physica B **259-261**, 608–613 (1999).

[24] W. G. Clark, M. C. Lan, G. van Kalkeren, W. H. Wong, C. Tien, D. E. MacLaughlin, J. L. Smith, Z. Fisk and H. R. Ott, J. Magn. Magn. Mater. **63-64**, 396 (1987).

[25] C. Tien and I. M. Jiang, Phys. Rev. B **40**, 229 (1989).

[26] E. T. Ahrens, R. H. Heffner, P. C. Hammel, A. P. Reyes, J. D.Thompson, J. L. Smith and W. G. Clark, Phys. Rev. B **59**, 1432 (1999).

[27] J. E. Sonier, R. H. Heffner, G. D. Morris, D. E. MacLaughlin, O. O. Bernal, J. Cooley, J. L. Smith and J. D. Thompson, Physica B **326**, 414 (2003).

[28] Takahiko Tsugawa. Master's thesis, Graduate School of Science, Hiroshima University, (2006).

[29] J. Bardeen and M. J. Stephen, Phys. Rev. **140**, A1197 (1965).

[30] Y. Matsuda, A.Shibata, K. Izawa, H. Ikuta, M. Hasegawa and Y. Kato, Phys. Rev. B **66**, 014527 (2002).

[31] Y. Tsuchiya, K. Iwaya, K. Kinoshita, T. Hanaguri, H. Kitano, A. Maeda, K. Shibata, T. Nishizaki and N. Kobayashi, Phys. Rev. B **63**, 184517 (2001).

[32] G. M. Schmiedeshoff, Z. Fisk and J. L. Smith, Phys. Rev. B **48**, 16417 (1993).

[33] N. B. Kopnin and A. V. Lopatin, Phys. Rev. B **51**, 15291 (1995).

[34] N. B. Kopnin and G. E. Volovik, Phys. Rev. Lett. **79**, 1377 (1997).

[35] J. P. Brison, O. Laborde, D. Jaccard, J. Flouquet, P. Morin, Z. Fisk, and J. L. Smith, J. Phys. France **50**, 2795 (1989).

[36] M. R. Norman, W. E. Pickett, H. Krakauer and C. S. Wang, Phys. Rev. B **36**, 4058(R) (1987).

[37] P. Gegenwart, C. Langhammer, R. Helfrich, N. Oeschler, M. Lang, J. S. Kim, G. R. Stewart and F. Steglich, Physica C **408-410**, 157 (2004).

[38] A. Hiess, A. Schneidewind, O. Stockert and Z. Fisk, Phys. Rev. B **89**, 235118 (2014).

[39] D. L. Cox, Phys. Rev. Lett. **59**, 1240 (1987).

[40] S. Nishiyama, H. Matsuura and K. Miyake, J. Phys. Soc. Jpn. **79**, 104711 (2010).

[41] S. Nishiyama and K. Miyake, J. Phys. Soc. Jpn. **80**, 124706 (2011).

[42] Naoyuki Miura. private communications.

[43] T. Tayama, T. Sakakibara, H. Sugawara, Y. Aoki and H. Sato, J. Phys. Soc. Jpn. **72**, 1516 (2003).

[44] R. H. Heffner, D. W. Cooke, A. L. Giorgi, R. L. Hutson, M. E. Schillaci, H. D. Rempp, J. L. Smith, J. O. Willis, D. E. MacLaughlin, C. Boekema, R. L. Lichti, J. Oostens and A. B. Denison, Phys. Rev. B **39**, 11345 (1989).

[45] D. Parker, O. V. Dolgov, M. M. Korshunov, A. A. Golubov and I. I. Mazin, Phys. Rev. B **78**, 134524 (2008).

[46] A. V. Chubukov, D. V. Efremov and I. Eremin, Phys. Rev. B **78**, 134512 (2008).

[47] K. Takegahara and H. Harima, Physica B **281-282**, 764 (2000).

[48] T. Maehira, A. Higashiya, M. Higuchi, H. Yasuhara and A. Hasegawa, Physica B **312-313**, 103 (2002).

[49] G. E. Volovik and L. P. Gor'kov, JETP **61**, 843 (1985).

[50] E. I. Blount, Phys. Rev. B **32**, 2935 (1985).

[51] M. Sigrist and K. Ueda, Rev. Mod. Phys. **63**, 239 (1991).

[52] M. Ozaki, K. Machida and T. Ohmi, Prog. Theor. Phys. **74**, 221 (1985).

Acknowledgments

First of all, I am deeply grateful to Professor Hideki Tou for a lot of advice, valuable discussions and continuous encouragements throughout the present work. I would like to thank Professor Hisashi Kotegawa for experimental support and valuable discussions. I would like to thank Professor Hisatomo Harima in Kobe university for valuable suggestions and discussions from theoretical view point.

I would like to thank Professor Yoshichika Ōnuki(University of Ryukyus), Dr. Yoshinori Haga and Dr. Etsuji Yamamoto (Japan Atomic Energy Agency) for providing us a high-quality single crystal.

I would like to thank Professor Dai Aoki, Professor Fuminori Honda, Dr. Yoshiya Homma, Dr. Dexin Li, Dr. Yusei Shimizu and Dr. Ai Nakamura in Tohoku University for providing Th doped (U,Th)Be_{13}, experimental supports and valuable discussions.

I would like to thank Professor Hiroshi Amitsuka, Dr. Tatsuya Yanagisawa, Dr. Hiroyuki Hidaka and Dr. Naoyuki Miura in Hokkaido university for providing $LaBe_{13}$ and valuable discussions..

I would like to thank all members of Tou laboratory for their useful discussions and cooperations throughout the present work.

Finally, I would like to express my gratitude to all my family and friends.